POLITECNICO DI TORINO

Master Degree course in Biomedical Engineering Biomedical Instrumentation

Master Degree Thesis

Experimental Analysis of Inferior Vena Cava Diameter Variations under Controlled Respiratory Load

Supervisors
Prof. Luca Mesin
Dr. Piero Policastro

Candidates
Giada Bronda
Adele Crapiz

Academic Year 2024-2025

Acknowledgements

We would like to express our sincere gratitude to Prof. Luca Mesin for his guidance, support, and supervision throughout this thesis. His experience and helpful suggestions were important in shaping our work and improving our understanding of the topic.

We are also very grateful to Dr. Piero Policastro, whose availability, practical advice, and constant help greatly contributed to the progress of this project. His support during both the experimental and analytical parts has been truly valuable.

We would also like to thank all the people who took part in the acquisitions and kindly volunteered for our experiments, as well as our families for their continuous support.

Abstract

Ultrasonography of the inferior vena cava (IVC) is a non-invasive technique widely employed to assess venous diameter and pulsatility, providing clinically relevant information on intravascular volume status and right atrial pressure (RAP). In routine clinical practice, this evaluation is based on non-standardized respiratory manoeuvres, such as the sniff test, which can limit measurement reproducibility and clinical reliability.

This thesis aims to investigate IVC behaviour under controlled inspiratory conditions by combining real-time ultrasonography with simultaneous spirometric acquisition. The experimental setup integrates a custom 3D-printed spirometer with a mechanical airflow resistance designed for this study. The resistance was designed using Autodesk Fusion 360 and printed in PET plastic. It consists of a cylindrical shell with a rotating internal disk featuring a 1 mm central hole. This geometry generates controlled airflow resistance while allowing minimal flow to keep the epiglottis open, ensuring effective transmission of pressure changes to the thoracic cavity. The rotation of the disk allows two configurations: open, corresponding to spontaneous breathing, and resisted, where the airflow passes only through the small central hole, increasing respiratory effort.

The experimental protocol consists of a 6-second inspiratory trial, divided into two equal phases: the first 3 seconds without resistance and the last 3 with resistance. This design enables the comparison of IVC dynamics before and after the application of an inspiratory load while maintaining a natural, continuous breathing pattern. The acquisition was tested both in supine and PLR (Passive Leg Raising) positions. Ultrasound recordings of the IVC in the longitudinal axis are acquired using the Viper software in real-time mode, allowing continuous segmentation of the venous diameter throughout the acquisition. Simultaneous spirometric data provide complementary information on flow and pressure variations, ensuring precise temporal alignment between respiratory and ultrasound signals.

The results show a consistent reduction in the inferior vena cava (IVC) diameter following the application of respiratory resistance across all subjects, with a negative diameter variation (ΔD post–pre) ranging between approximately -1 mm and -5 mm. The Caval Index (CI), which quantifies diameter variability, has higher values in the supine condition (normal), about 30-60%, compared to the PLR condition, where it was about 10-45%. These observations highlight an increased respiratory collapsibility of the IVC during spontaneous breathing, whereas the PLR posture enhances venous return, promoting vessel stabilization and reducing oscillatory behaviour.

In conclusion, controlled inspiratory resistance induces a measurable reduction in IVC diameter, reflecting the rise in intrathoracic pressure. The PLR condition mitigates this effect by increasing preload and minimizing collapsibility. These findings suggest that the combination of standardized respiratory loading and postural modulation can improve the physiological interpretation and reproducibility of IVC-based hemodynamic evaluations.

Contents

List of Figures

List of Tables

Chapter 1

Introduction

Assessment of hemodynamic variables is a key component in the treatment of patients with advanced heart failure or severe liver disorders. Among the major vascular structures, the Inferior Vena Cava (IVC), the largest vein in the human body, is of particular interest because its diameter and mechanical behaviour can mirror changes in central venous pressure (CVP) and right atrial pressure (RAP). Due to its considerable calibre, the IVC can accommodate large blood volumes, and its marked compliance makes it especially responsive to variations in both intrathoracic and intra abdominal pressures.

Ultrasonography is the preferred non-invasive technique for assessing the IVC, as it enables real-time monitoring of its diameter and the way it changes over time. One of the most frequently reported parameters is the Caval Index (CI), which expresses the percentage change in IVC diameter across the respiratory cycle and serves as an indirect estimate of CVP, as well as a predictor of fluid responsiveness. Although right heart catheterization remains the clinical gold standard for direct RAP measurement, its invasive nature limits its practical use. In comparison, ultrasound provides a safer, faster and more accessible option [1].

Although IVC ultrasonography holds considerable clinical value, its use is constrained by notable limitations. The reliability and consistency of the measurements can be reduced by multiple sources of variability, including inter-subject physiological differences, the operator's ability to maintain optimal probe alignment, and fluctuations in the patient's breathing pattern. These factors can significantly affect the reproducibility of the observed diameter changes, limiting the diagnostic and monitoring potential of this technique.

To mitigate these issues, recent research has explored the adoption of standardized breathing protocols combined with semi-automated image analysis tools, such as VIPER, with the aim of enhancing the objectivity and repeatability of IVC assessment [2]. Building on these premises, the present work focuses on identifying a respiratory condition that enables reproducible and reliable measurements of IVC diameter variation.

Specifically, controlled breathing trials were designed to reduce variability in respiratory mechanics while maintaining physiological realism. Ultrasound and spirometry data were acquired simultaneously under different experimental conditions, and the resulting signals were processed through automated analysis pipelines to quantify and compare the consistency of IVC diameter changes across repetitions and subjects.

The overarching aim of this study is to contribute to the development of a robust and standardized protocol for IVC ultrasonography, intended to reduce measurement variability and enhance the reliability of clinical assessments. The following chapters outline the physiological and methodological background that frames the investigation, describe in detail the acquisition setup, signal processing, and analysis procedures, and finally discuss the results in relation to their clinical relevance and prospective applications.

Chapter 2

Scientific and technical background

A comprehensive evaluation of IVC as a marker for RAP and CVP requires a detailed understanding of its anatomical structure and its functional relationships with both the cardiovascular and respiratory systems [3].

This chapter also outlines the fundamental physical principles underlying ultrasonography, with a focus on its use in vascular imaging [4].

2.1 Cardiovascular system

The cardiovascular system consists of the heart, blood vessels, and blood. Its primary function is to transport nutrients and oxygenated blood to all parts of the body and to carry deoxygenated blood to the lungs.
The **heart** is a muscular organ that pumps oxygenated blood to the systemic circulation and deoxygenated blood to the lungs for gas exchange. It is located within the mediastinum, between the two lungs and slightly to the left of the midline.

The **heart wall** is composed of three layers: the endocardium, the inner layer that covers the internal chambers and valves. It provides a smooth lining for efficient blood flow; the myocardium, which consists of involuntary striated muscle and generates the force to pump blood through the body; and the epicardium, the outermost layer that protects the myocardium. The muscular body of the heart is surrounded by the pericardium, a fluid-filled fibrous sack that prevents overfilling and reduces friction generated by the heart's movement. The heart is divided into two halves, right and left heart. Each half is composed of two chambers, the atrium, a thin walled chamber that receives blood from the veins, and the ventriculum, a thicker walled chamber that pumps blood into the arteries.

Four **valves** regulate the direction of blood flow and prevent backflow during the car- diac cycle. The atrioventricular valves (AV), tricuspid and mitral valves, are located bewteen the atria and ventricles and allow blood flow from the upper chambers to the lower chambers. The semilunar valves (SV), pulmonary and aortic valves, are positioned at the exits of the ventricles and open during ventricular contraction to enable ejection of blood into the pulmonary artery and the aorta.

Blood vessels are tubular structures that originate and terminate at the heart. This network ensures the delivery of nutrients and oxygen while simultaneously collecting carbon dioxide and other waste products from the tissues.
Blood is a complex fluid responsible for carrying respiratory gases, nutrients, hormones, and metabolic by-products, regulating the body's temperature, and maintaining the balance of fluids. It has four main components: plasma, red blood cells, white blood cells, and platelets.

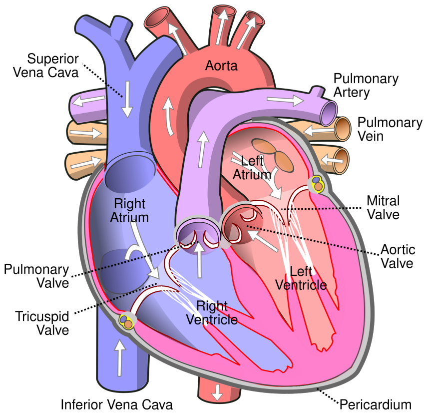

Figure 2.1: Anatomy of the heart.

2.1.1 Blood vessels

Blood vessels are tubular structures responsible for carrying blood to and from the heart. They are active and dynamic organs, capable of contracting and expanding to maintain blood pressure and regulate blood flow.

Blood vessels classification

Based on their function and structure, blood vessels are classified into arteries, veins, and capillaries.

- Arteries are muscular vessels that carry oxygenated blood from the heart to the tissues. To resist the high pressure generated by the blood flow, they are characterized by thick walls. Arteries branch out into smaller vessels called arterioles. The main arteries that originate from the heart are the aorta and the pulmonary arteries.

- Veins carry deoxygenated blood from the body to the heart. To facilitate venous return and compensate for the low pressure, veins have a wider lumen and thinner walls compared to arteries. They are also equipped with valves that prevent the backflow of blood. Venules merge into veins, which eventually form the superior and inferior vena cava and the pulmonary veins.

- Capillaries are the smallest vessels, with thin and single-layered endothelial walls. Their function is the exchange of oxygen and waste products with surrounding tissues, which is facilitated by their reduced dimension. Oxygen and nutrients diffuse from the blood to the tissues, while carbon dioxide and waste products diffuse from tissues to the blood.

Inferior Vena Cava

The IVC is the largest vein in the human body and is responsible for transporting deoxygenated blood from the lower extremities and abdominal organs to the right atrium. Anatomically, it is formed by the convergence of the right and left common iliac veins and is positioned posterior to the abdominal cavity, to the right of the aorta.

With an approximate diameter of 30 mm, the IVC is a highly compliant vessel, meaning that its cross-sectional area changes in response to pressure and volume variations. This makes it an effective indicator of central venous pressure. In states of low CVP, the IVC exhibits high collapsibility and may assume an elliptical shape [5].

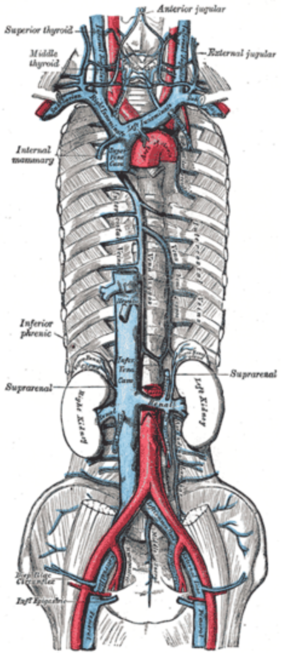

Figure 2.2: Inferior Vena Cava anatomy

2.1.2 Cardiac cycle

The cardiac cycle refers to the sequence of alternating contraction and relaxation of the atria and ventricles that results in pressure changes within the heart. These variations lead to blood movements from atria to ventricles and from ventricles to the system. It consists of two main phases: diastole, the relaxation phase, and systole, the contraction phase.

- **Diastole**: relaxation of the heart muscle. In this phase, blood returns through systemic veins from the body to the right atrium and from the lungs to the left atrium. The pressure in the atria increases, exceeds the pressure in the ventricles, and causes the AV valves to open. Blood starts flowing passively from the atria to the ventricles resulting in a ventricular filling. The ventricular pressure is lower than the pressure in the arteries, and the semilunar valves are closed.
- **Atrial systole**: Ventricular filling mostly occurs passively during diastole, although the contraction of the atria ensures that the remaining blood is fully pushed into the lower chambers. After contraction, atrial pressure decreases, leading the AV valves to close. This phase ensures the ventricles are filled to their optimal capacity, enhancing cardiac efficiency.
- **Ventricular systole**: the ventricular muscles contract, leading to an increase in ventricular pressure. The initial phase of the contraction is called iso-volumetric contraction, during which both AV valves and semilunar valves are closed. The closing of the valves causes a rise in ventricular pressure without altering the blood volume.
  When the ventricular pressure exceeds the arterial pressure, the semilunar valves open, allowing the ejection of blood from the ventricles to the arteries. The right ventricle pumps blood through the pulmonary valve to the lungs, and the left ventricle through the aortic valve to the rest of the body.

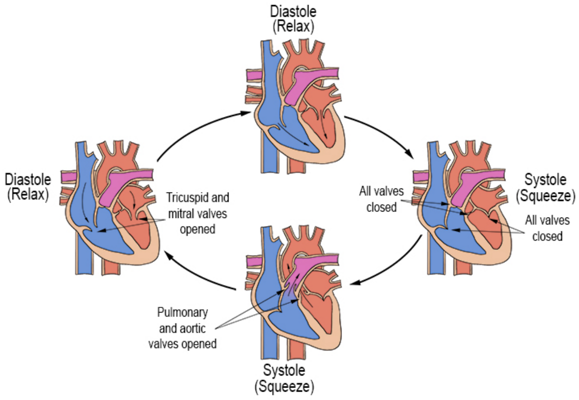

Figure 2.3: Cardiac cycle

2.1.3 Influence of the cardiac cycle on the Inferior Vena Cava

The IVC is highly sensitive to the cardiac cycle because of its thin and compliant walls. Its motion and diameter variations are influenced not only by respiratory mechanics but also by the hemodynamic effects of blood flow and pressure changes generated by cardiac activity. As a result, the vein is highly responsive to pulsatile changes in venous return and right atrial pressure [1].

During ventricular systole, the contraction of the right ventricle causes the RAP to rise temporarily, leading to distension of the IVC and an observable increase in diameter. During diastole, the relaxation of the atrium and ventricle favors venous return, resulting in a decrease of RAP and reduction of the IVC diameter.
The amplitude of these variations is modulated by the volemic status and CVP of the patient; in hypovolemic patients, the IVC collapsibility and the sensitivity to pressure increase, while in hypervolemic conditions, the vessel remains distended and the variations of the diameter are less evident [6].

2.2 Respiratory system

The respiratory system consists of the organs that allow us to breathe and sustain the continuous exchange of gases between the body and the external environment. Its primary role is to deliver oxygen to tissues and remove carbon dioxide.
Structurally, this system is organized as a network of airways that guide air from the environment to the lungs. These include the nasal and oral cavities, the pharynx, larynx, trachea, and bronchial tree. The smallest branches end up in clusters of alveoli, microscopic sacs surrounded by capillaries, where oxygen and carbon dioxide move through the alveolar wall by diffusion.

The principal muscles involved in the mechanism of respiration are the diaphragm and the intercostal muscles. Through their coordinated action, these muscles generate cyclic changes in the thoracic volume. During inspiration, these muscles contract and expand the thoracic cavity, allowing an increase in lung and alveolar volumes. The increase in volume causes a drop in alveolar pressure, generating a pressure gradient that allows air to flow into the lungs. During expiration, muscles relax and the thoracic cavity and lungs return to their resting state, raising the alveolar pressure and causing air to be expelled.

As air enters the body through the nostrils, it travels along the nasal cavity, where it is filtered, humidified, and warmed. From there, it passes through the pharynx and larynx to the trachea, which bifurcates into the two primary bronchi that enter the lungs. The bronchi progressively branch into narrower bronchioles that finally open into the alveolar sacs, the alveoli, where gas exchange occurs.

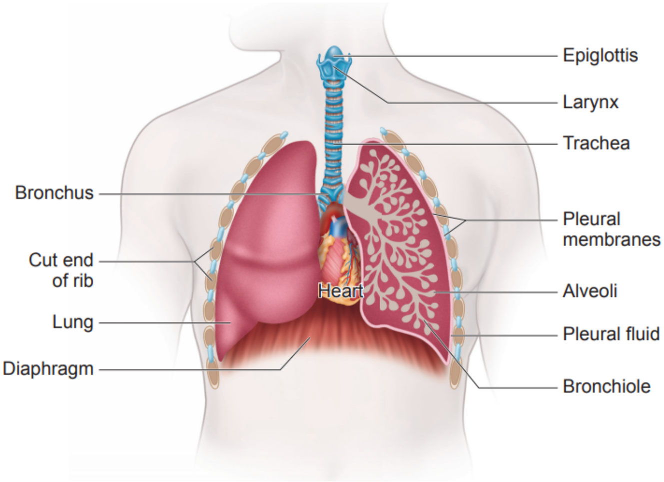

Figure 2.4: Anatomy of the respiratory system

2.2.1 Respiratory cycle

The respiratory mechanism is described by Boyle's law, which states that the pressure of a gas is inversely proportional to its volume when the temperature remains constant. As the volume of the lungs changes the intrapulmonary pressure varies accordingly, creating pressure gradients that drive air movement.

During **inspiration** coordinated contraction of the diaphragm and intercostal muscles causes expansion of the thoracic cavity, increasing lung and alveolar volumes. Consequently, their internal pressure decreases below atmospheric pressure, allowing air to flow into the alveoli until pressure equilibrium is restored.
This phase directly influences blood flow: the drop in intrathoracic pressure, combined with a rise in intra-abdominal pressure, enhances venous return from the abdominal veins towards the thoracic cavity. This mechanism facilitates venous return and contributes to the filling of the right atrium.

During **expiration**, the respiratory muscles relax and the thoracic cavity decreases in volume, leading to compression of the lungs and increased alveolar pressure. This creates an opposite pressure gradient, causing air to flow outward. The reduced pressure difference between the abdominal and thoracic compartments reduces venous return to the heart.

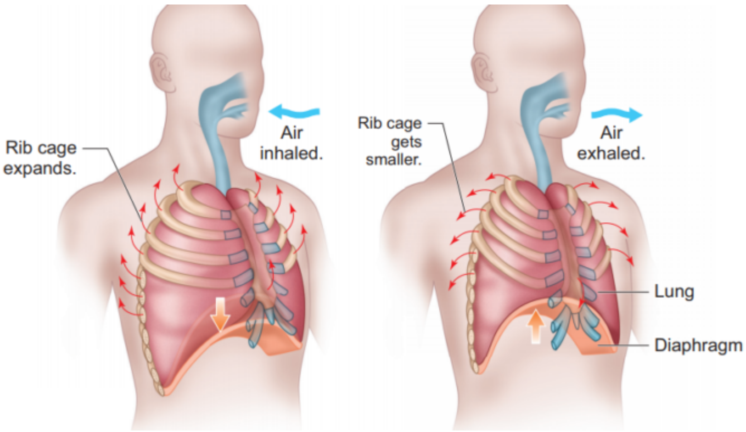

Figure 2.5: Respiratory mechanics

2.2.2 Respiratory volumes and capacities

Lung volumes describe the amount of air contained within the lungs during specific phases of the respiratory cycle. Each volume reflects a specific mechanical aspect of breathing and contributes to the assessment of pulmonary function:

- **Tidal Volume (TV)**: the amount of air that enters or leaves the lungs during a single, unforced respiratory cycle. In healthy adults at rest, this value ranges between 300 mL and 500 mL.
- **Inspiratory Reserve Volume (IRV)**: the additional volume that can be inspired through maximal effort after a normal inspiration, generally 3000 mL.
- **Expiratory Reserve Volume (ERV)**: the additional volume that can be expelled after a normal expiration, usually around 1000 mL.
- **Residual Volume (RV)**: the quantity of air remaining in the lungs after maximal expiration, preventing alveolar collapse, approximately 1200 mL.

Pulmonary capacities represent the total amount of air that the lungs can hold and are derived from combinations of individual volumes, and provide a broader picture of the mechanical limits of the respiratory system:

- **Inspiratory capacity (IC)**: the greatest amount of air that can be inhaled following a normal expiration; $IC = TV + IRV$.
- **Vital capacity (VC)**: the total volume of air that can be exhaled after a maximal inhalation; $VC = TV + IRV + ERV$.
- **Functional residual capacity (FRC)**: the volume of air remaining in the lungs at the end of a normal expiration; $FRC = ERV + IRV$.
- **Total lung capacities (TLC)**: the total volume of air contained in the lungs after a maximal inspiration; $TLC = TV + IRV + ERV + RV$.

Lung volumes and capacities vary among subjects, due to factors as age, sex, height, weight, ethnicity, and level of physical activity [7].

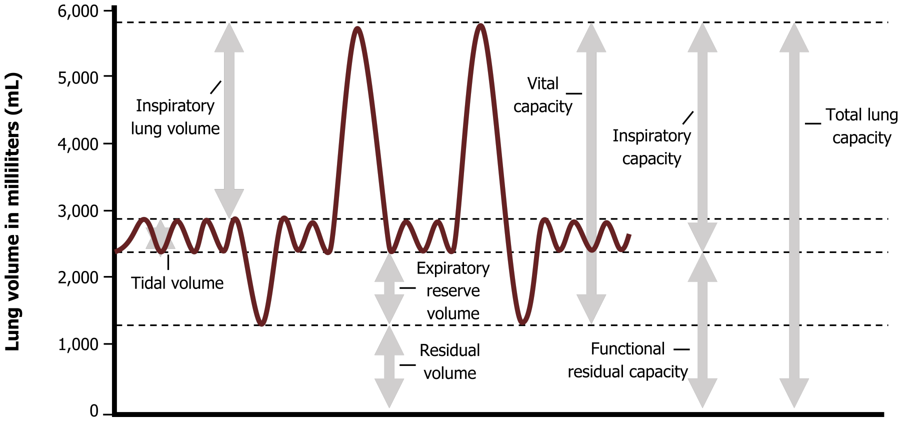

Figure 2.6: Respiratory volumes and capacities

2.2.3 Respiratory Influence on IVC Dynamics

Respiration manages venous return and, consequently, the diameter of the Inferior Vena Cava (IVC). Cyclical shifts in intrathoracic and intra-abdominal pressures modify the pressure gradient between the peripheral veins and the right atrium.

During inspiration, contraction of the diaphragm and intercostal muscles lowers intrathoracic pressure, while the descent of the diaphragm compresses the abdominal contents, increasing intra-abdominal pressure. This combination augments the venous return from the abdominal compartment toward the thorax, producing a transient reduction of the IVC diameter on ultrasound imaging.

During expiration, the respiratory muscles relax, the pressure gradient slows venous return, allowing the IVC to expand and reach its maximal dimension. The magnitude of these diameter oscillations depends on the depth and pattern of breathing: deep or resistive inspirations increase the pressure differential and amplify collapsibility, whereas shallow or irregular breathing produces smaller changes. These "respiratory-venous" interactions are well-described physiologically, and this is why dynamic IVC indices are used as substitutes for RAP and intravascular volume status [8].

Through these mechanisms, the respiratory cycle continuously modulates the filling dynamics of the right atrium. Consequently, the degree of IVC collapsibility provides an indirect indication of central venous pressure and general intravascular volume status, linking respiratory mechanics to hemodynamic regulation.

2.3 Spirometry

Spirometry is a widely adopted test for the quantitative assessment of pulmonary function. Provides an objective evaluation of the mechanical performance of the lungs by measuring the volumes of air inhaled and exhaled during specific breathing maneuvers. It is a non-invasive and relatively simple procedure, suitable for both healthy individuals and patients with respiratory conditions, both in clinical and research contexts.

The test is performed using an instrument known as a **spirometer**, which typically consists of a mouthpiece connected to a flow or volume transducer that converts respiratory movements into electrical signals. The data is transmitted to a computerized system that processes, displays, and analyzes the results in real time.

One of the primary outcomes of spirometry is VC measurement; there are also parameters like the Forced Expiratory Volume (FEV) and the Forced Vital Capacity (FVC), both obtained during a maximal forced expiration.
Spirometry can directly measure several static lung volumes and capacities, including Tidal Volume (VT), Inspiratory Reserve Volume (IRV), Expiratory Reserve Volume (ERV), Inspiratory Capacity (IC) and Vital Capacity (VC). However, spirometry cannot measure the Residual Volume (RV), which is the amount of air that remains in the lungs after a maximal exhalation, as it cannot be expelled and therefore cannot be recorded directly.

The raw data collected from a spirometer can be graphically displayed as a volume-time curve, representing the amount of air exhaled as a function of time and providing insight into both the dynamics and static properties of the respiratory system.

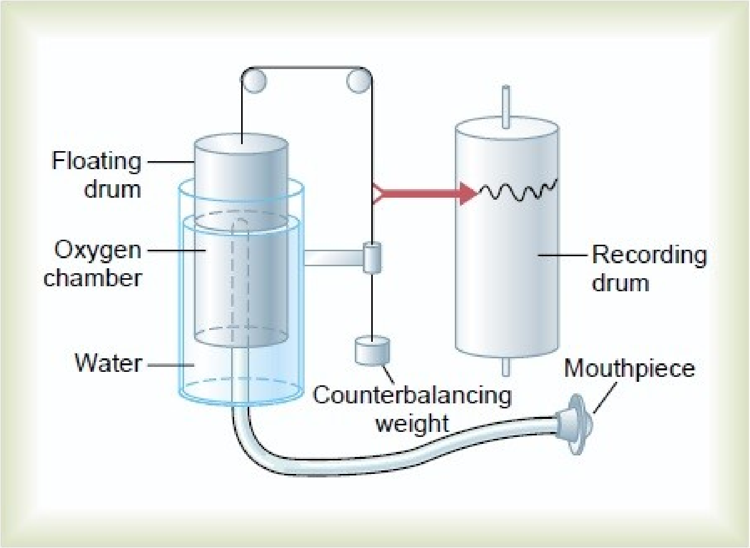

Figure 2.7: Hutchinson’s spirometer

2.4 Ultrasonography

Ultrasonography is a medical imaging technique that utilizes ultrasound, a form of high-frequency sound waves that convey mechanical energy through biological tissue. When ultrasound encounters interfaces between different materials, part of the energy is reflected and detected by the transducer, allowing image reconstruction. In its most common clinical application, it provides real-time, two-dimensional, grayscale images that allow visualization of both anatomical structures and dynamic physiological processes.

This imaging technique is widely used in clinical and research settings due to its characteristics. Ultrasound uses a non-ionizing form of radiation, meaning that it does not induce cellular or genetic damage. As such, it is safe for repeated and long-term use, even in vulnerable patient populations, such as pregnant patients.

Its high temporal resolution, up to 300 frames per second, allows the capture of fast physiological phenomena, such as cardiac motion, vascular wall pulsation, or respiratory-induced variations, making it an ideal tool for dynamic functional evaluation in cardiovascular and respiratory studies [9].

2.4.1 Physical principles and characteristics of ultrasonography

Ultrasound refers to sound waves with frequencies above the audible range, typically ranging from 2 to 20 MHz in medical imaging. Waves propagate through tissue by alternating phases of compression and rarefaction, transmitting mechanical energy throughout the medium. One of the main advantages of ultrasound is its ability to focus the beam on a specific region of interest, enhancing spatial resolution and enabling detailed visualization of small structures.

The propagation of the ultrasound waves depends on the physical properties of the medium, its density and compressibility, which determine the local speed of sound. Variations in these parameters among different tissues are essential for image formation, as they give rise to reflections and refractions that can be detected and interpreted by the imaging system.

The generation and detection of ultrasound waves is based on the **piezoelectric effect**, a property of certain materials to convert electrical energy into mechanical vibrations, and vice versa. Specific anisotropic crystals, such as quartz and synthetic ceramics exploit this phenomenon.

The piezoelectric effect can be described through two complementary mechanisms:

- **Direct piezoelectric effect**: mechanical deformation of the crystal generates an electrical potential across its surfaces.

- **Inverse (indirect) effect**: external application of an electric potential induces mechanical deformation of the crystal.

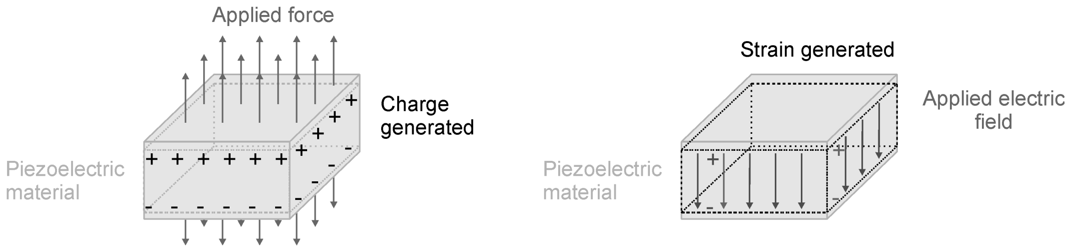

Figure 2.8: Piezoelectric effects: A) direct piezoelectric effect, B) inverse piezoelectric effect.

In medical ultrasonography, the inverse effect is used to emit acoustic pulses, while the direct effect is used to detect echoes reflected from tissue interfaces. Currently, piezoelectric transducers typically employ lead zirconate titanate (PZT) ceramics because of their high electromechanical coupling efficiency, stability, and durability.

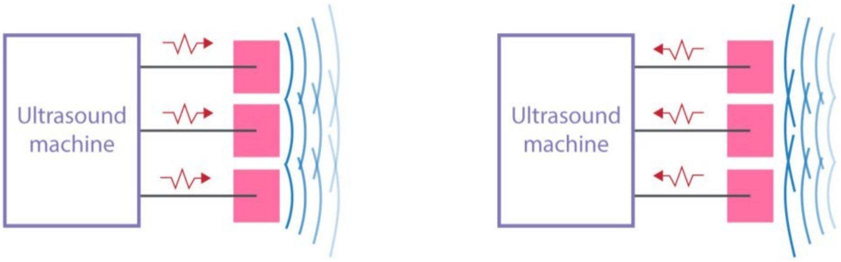

Figure 2.9: Transducer: A) emission of ultrasound waves, B) reception of reflected waves.

Since the same transducer element acts as both transmitter and receiver, emission is performed in short bursts, leaving sufficient time for receiving the returning echoes before the next pulse is generated. The piezoelectric crystal acts as a **mechanical resonator**, vibrating most efficiently at a specific frequency. Resonance occurs when the crystal thickness is equal to half the wavelength of the emitted ultrasound.

The speed of propagation of an ultrasound wave in a medium is defined by the product of its wavelength λ and its frequency f:

$$v = \lambda \cdot f$$

where:

- v is the propagation speed [m/s],
- λ is the wavelength [m],
- f is the frequency [Hz].

Wavelength directly influences spatial resolution: shorter wavelengths and higher frequencies produce better spatial resolution but are more attenuated, limiting the penetration depth of the ultrasound beam. A balance between frequency and depth must be selected depending on the clinical or experimental application.

A critical parameter for ultrasound-tissue interaction is the **acoustic impedance**, defined as:

$$Z = \rho \cdot v$$

where:

- ρ is the density of the medium [kg/m^3],
- v is the propagation speed [m/s].

Acoustic impedance quantifies the resistance of a medium to the passage of sound waves. The difference in acoustic impedance between two adjacent tissues determines how much of the wave is reflected or transmitted at the interface. High impedance mismatch results in stronger echo, which is fundamental in ultrasound imaging to create contrast between different structures.

2.4.2 Ultrasound attenuation and resolution

As an ultrasound wave propagates through a medium, it gradually loses energy due to absorption and scattering. This phenomenon, known as attenuation, depends on the physical properties of the medium and can be mathematically described by the exponential decayfunction:

$$A(z) = A_0 \cdot e^{-\alpha \cdot z}$$

Where:

- A_0 is the initial amplitude of the ultrasound wave,
- α is the attenuation coefficient of the medium [Np/m],
- z is the depth of propagation [m].

Attenuation is highly frequency-dependent. As the frequency of the ultrasound increases, the resolution of the image improves due to shorter wavelengths, but the attenuation also increases, limiting penetration depth. Conversely, lower frequencies attenuate less and can reach deeper structures, but at the cost of reduced spatial resolution.

For this reason:

- **High-frequency ultrasound** (e.g., 10-15 MHz) is used for imaging superficial structures such as tendons, skin, and vessels;
- **Low-frequency ultrasound** (e.g., 2-5 MHz) is used for abdominal and deep organ imaging.

The optimal imaging frequency is always a trade-off between image resolution and penetration depth.

2.4.3 Ultrasound image generation

Ultrasound imaging is based on the emission of short pulses of sound waves into the body and the analysis of the echoes reflected from tissue interfaces. When an acoustic pulse encounters a boundary between media with different acoustic impedance, part of the energy is reflected and returns to the transducer as an echo.

The depth of the reflecting structure is calculated from the *time of flight* of the echo, defined as:

$$\Delta t = \frac{2d}{c}$$

where

- Δt is the total time taken for the wave to travel to the target and back [s],
- d is the distance from the transducer to the reflecting interface [m],
- c is the speed of sound in the medium [m/s].

Since the wave must travel to the target and back, the measured time corresponds to twice the actual depth. By emitting successive pulses along predefined scan lines and measuring the amplitude and timing of each returning echo, the device reconstructs a two-dimensional map of acoustic reflectivity.

The main components involved in ultrasound image generation are:

- a piezoelectric transducer that generates and receives the acoustic pulses,
- a signal amplifier to boost the weak returning echoes,
- a processing unit to convert the signals into an interpretable image.

To account for the fact that deeper tissues return weaker signals due to attenuation, the system applies **Time Gain Compensation (TGC)**. This dynamic amplification increases with echo delay time, equalizing the intensity of echoes received from various depths.

After compensation, the amplitude of each echo is mapped to a grayscale value: stronger echoes appear brighter, while weaker ones appear darker. The final image displayed on screen is thus a real-time 2D cross-sectional view of internal tissue structures.

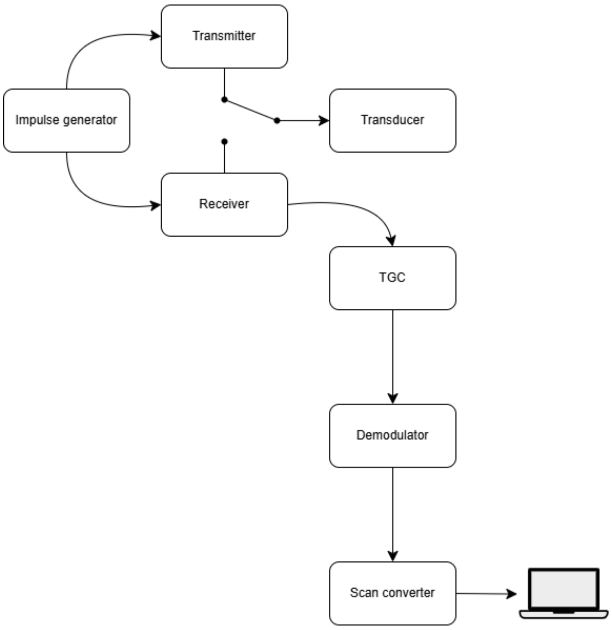

Figure 2.10: Flowchart of ultrasound image generation.

2.4.4 Structure of ultrasound devices

An ultrasound scanner is a diagnostic imaging device that generates real-time images of internal anatomical structures using high-frequency sound waves.

The system is composed of three main functional components:

- **The probe (transducer)**: This is the physical interface between the imaging system and the patient. It contains an array of piezoelectric crystals, each connected via dedicated wiring that allows for both transmission and reception of acoustic signals. The wires are organized within a cable that connects the probe to the central processing unit. The probe's geometry and frequency range determine its imaging depth and resolution.

- **The impulse generator (pulser)**: Also referred to as the transmitter, this unit produces high-voltage radio-frequency (RF) electrical pulses, typically in the range of 1 to 20 MHz, that excite the piezoelectric crystals within the probe. These pulses generate the ultrasound waves that propagate through the body. The timing and sequence of these pulses are precisely regulated to direct and concentrate the beam, allowing the device to achieve dynamic focusing [10].

- **The electronic processing unit**: this module processes the electrical signals generated by the transducer as it converts the returning acoustic waves back into electrical echoes. These signals are first amplified and filtered to enhance the signal-to-noise ratio, and then digitized through analog-to-digital conversion. The processed signals are subsequently converted through the application of delay-and-sum beamforming algorithms, envelope detection, and logarithmic compression to obtain a two-dimensional grayscale image, representing the amplitude of the reflected echoes. The resulting image is displayed on a screen in real-time, enabling the visualization of moving structures such as cardiac chambers, vessel walls, or respiratory excursions.

These components work in a time-multiplexed manner, allowing for continuous switching between transmission and reception modes. Effective synchronization is crucial to avoid interference between emitted and received signals, ensuring precise temporal sampling of echoes and enabling frame-by-frame reconstruction of dynamic biological activities. Integration of these functions within compact, portable devices has significantly expanded the applicability of ultrasound imaging, allowing its transition from traditional hospital settings to bedside evaluations and point-of-care diagnostics.

Figure 2.11: Ultrasound imaging system.

2.4.5 Ultrasound probes

Modern ultrasound probes consist of arrays of piezoelectric elements that convert electrical signals into acoustic waves and vice versa. Their geometric configuration determines the shape, directionality, and focus of the emitted ultrasound beam. The selection of the appropriate probe depends primarily on the anatomical region of interest, the required imaging depth, and the desired resolution.

Different probe geometries have been developed to improve imaging performance for both clinical and research purposes:

- **Linear probe**: the piezoelectric crystals are arranged in a straight line, producing a rectangular image field. These probes operate at relatively high frequencies (typically 5-20 MHz). Their penetration depth is limited, making them suitable for imaging superficial structures such as tendons, muscles, the thyroid, and vessels. They are used in vascular ultrasonography and musculoskeletal diagnostics.

- **Convex (curvilinear) probe**: the elements are distributed along a curved surface, generating a sector-shaped field of view. Operating at lower frequencies (2-7 MHz), these probes are ideal for abdominal imaging and visualization of deep or large organs due to their wider field of view and increased penetration.

- **Phased array probe**: This probe uses electronic beam steering and focusing, achieved by applying phase delays to the excitation signals of each element. It is compact and operates in the 2-10 MHz range and produces a narrow sector-shaped image. Due to its compact design and high temporal resolution, this probe is useful in cardiac applications. It facilitates imaging through intercostal spaces while providing dynamic visualization of cardiac motion [10].

- **Endocavitary probe**: designed for internal examinations, such as transvaginal or transrectal imaging, these transducers provide close access to target organs while offering high spatial resolution. Operating at mid-to-high frequencies, they minimize signal attenuation due to their proximity to the target area, which enhances image clarity and detail. This makes them essential in gynecological, urological, and gastrointestinal ultrasonography.

Each probe design involves balancing spatial resolution, penetration depth, and field of view. Understanding these characteristics is crucial for selecting the appropriate configuration for a specific diagnostic or experimental purpose.

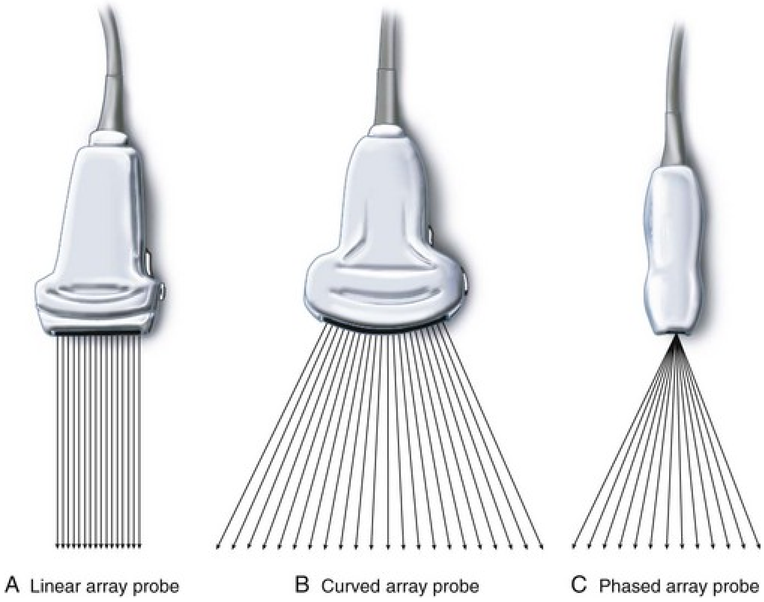

Figure 2.12: Different types of ultrasound scanning probes.

2.4.6 Ultrasound artifacts

Ultrasound artifacts are image distortions that are frequently observed in clinical practice and can lead to misinterpretation of anatomical structures. These artifacts arise from complex acoustic interactions, non-uniform sound propagation, or strong reflections at tissue interfaces. Understanding their source is crucial to avoid misinterpretation and maintain accurate measurements, especially in imaging of the IVC.

In this context, the most frequently observed artifacts include:

- **Reverberation**: This artifact appears as multiple, equally spaced linear echoes caused by repeated reflection of the ultrasound beam between two reflective parallel surfaces. In abdominal scans, reverberation can occur between the transducer face and the anterior wall of the IVC, causing artificial linear repetitions, which can distort the true contours of the vessel [11].
- **Comet-tail artifact**: A specific type of reverberation, it presents as a bright, narrowing trail extending backward from a reflective surface. It results from reverberations that occur within a small region, such as near microbubbles, and is observed adjacent to vessel walls or air-tissue boundaries [11].
- **Acoustic shadowing:** This appears as a dark or anechoic region distal to a strongly attenuating structure. It occurs when a dense interface (e.g., ribs, bone, gas, or calculus) absorbs or reflects most of the incident energy, reducing the amplitude of echoes returning from deeper tissues. In IVC subcostal imaging, this artifact, caused by ribs and gas from the intestine, often poses challenges by obstructing the visibility of the vessel lumen [12].
- **Mirror artifact**: this happens when the ultrasound beam hits a strong specular reflector (e.g., lungs or diaphragm), causing the echo to be redirected before returning to the transducer. The system interprets the delayed signal as a structure located deeper than its actual position, creating a mirrored duplication of the IVC or nearby organs [12].
- **Posterior acoustic enhancement (reinforcement)**: this artifact is characterized by increased echo brightness distal to fluid-filled structures (e.g., bladder, cysts). Since acoustic attenuation is minimal in fluids, more sound intensity reaches deeper tissues, resulting in brighter echoes and apparent hyperintensity in the posterior regions. In IVC imaging, this can enhance the visibility of posterior vessel walls or deeper hepatic tissue [12].
- **Side-lobe artifact**: Resulting from secondary ultrasound beams beyond the primary acoustic axis. Weaker beams can undergo reflection at robust interfaces, creating the illusion that originates along the main axis, creating faint "ghost" echoes within otherwise anechoic regions, such as vascular lumens.

Understanding these phenomena is essential for both qualitative and quantitative analyzes. Practical approaches to mitigate challenges include optimizing probe orientation, using intercostal acoustic windows to bypass ribs and gas interference, adjusting system gain and dynamic range to minimize low-level reflections, and validating suspected artifacts by changing the insonation angle or patient position. Additionally, the use of semi-automated diameter tracking algorithms has been proposed to limit the influence of transient artifacts in quantitative IVC analysis [13].

2.4.7 IVC echography

Ultrasonographic assessment of the IVC represents a simple and non-invasive method to evaluate venous return and right atrial filling dynamics. The examination can be performed using either a low-frequency curvilinear probe, typically used for abdominal imaging, or a phased-array probe, commonly used in echocardiography.

The patient is generally positioned supine on a hospital bed to facilitate access to the thorax and to minimize hydrostatic variations in venous pressure. The IVC can be visualized in either a longitudinal or transverse plane; however, in most cases, image acquisition is conducted using the longitudinal (sagittal) subcostal view, which provides an extended visualization of the IVC along its pathway towards the right atrium. In this approach, the probe is placed just below the xiphoid process, with the orientation marker directed cranially. This configuration allows for continuous monitoring of the vessel from its intrahepatic segment to the atriocaval junction, allowing precise assessment of respiratory-induced variations in its diameter.

Alternatively, the transverse view can be acquired by rotating the probe approximately 90 degrees, orienting the marker toward the patient's right side. This approach allows cross-sectional imaging of the vessel, useful for confirming IVC identification and assessing its circularity and absolute diameter under static conditions. Although the transverse view provides limited insight into dynamic motion, it serves as a complement to longitudinal imaging by helping to confirm proper probe alignment and the elimination of artifacts due to oblique insonation [14].

Maintaining consistent positioning of the probe and applying gentle pressure are crucial to avoid vessel compression, which can falsely decrease its apparent dimensions. Standardized acquisition protocols suggest taking measurements around 2-3 cm caudal to the right atrium, distal to where the hepatic veins enter, to ensure consistency among observers and between different phases of the breathing cycles [14].

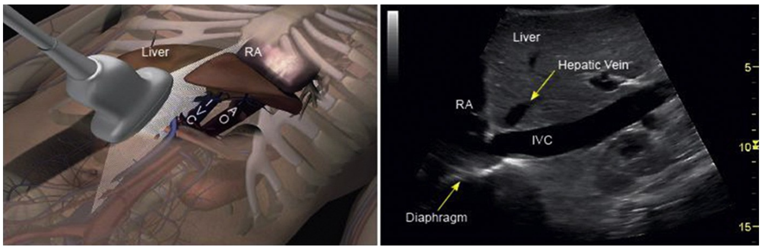

Figure 2.13: IVC echography: longitudinal view

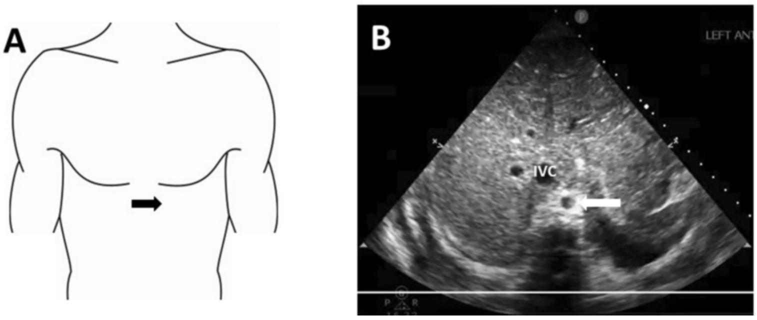

Figure 2.14: IVC echography: transverse view

2.5 Existing Methods and Experimental Studies

In clinical settings, inferior vena cava (IVC) ultrasonography is a well-established non-invasive approach commonly used to assess right atrial pressure (RAP) and volume status. It is typically performed using a subcostal longitudinal view, analyzing the IVC approximately 2-3 cm distal to its junction with the right atrium. This approach allows for continuous monitoring of the IVC during the respiratory cycle and measurement of its dynamic diameter variations [14, 15].

One of the most widely used parameters is the **Caval Index** (CI), which represents the percentage variation in the diameter of the IVC during the respiratory cycle. According to clinical guidelines from American and European sources, a CI greater than 50% combined with a maximum IVC diameter of less than 2.1 cm is indicative of normal RAP values, ranging between 0 to 5 mmHg. At the same time, an CI below 20% suggests elevated RAP [16]. These thresholds have been confirmed in multiple studies as reliable markers for assessing preload responsiveness and venous return, especially in emergency and critical-care settings [17].

Despite its clinical utility, IVC ultrasonography presents several limitations. Variations arise from both biological and technical factors (including differences in intrathoracic pressure, abdominal wall compliance, and breathing effort) as well as from the operator's experience and probe positioning. In particular, the reproducibility of the measurement is influenced by the operator, the patient's respiratory pattern, and probe angulation [15,18]. Voluntary respiratory effort, such as the sniff test or deep inhalation, increases venous collapse. Similarly, small probe movements caused by diaphragmatic activity or abdominal pressure can alter the measured size of the IVC [14]. Minor changes in the insonation angle or pressure applied by the transducer can alter the precise measurement of the diameter, potentially affecting the calculated CI [18].

To mitigate these issues, several methods have been proposed. Standardized acquisition protocols along with controlled breathing patterns have been implemented to reduce intra- and inter-subject variability [14, 17]. Similarly, computational methods have been developed to minimize operator dependence, including semi-automated techniques for vessel tracking employing active contour models. The VIPER framework, in particular, has played a significant role in recent experimental studies [13, 17]. These algorithms provide more reliable measurements of the diameter of the IVC over time, enabling the separation between respiratory and cardiac influences on venous pulsatility.

Integration of standardized acquisition methods with algorithmic analysis has significantly improved the reliability, objectivity, and reproducibility of IVC ultrasonography. This shift from traditional qualitative bedside evaluation to a more quantitative and automated imaging approach has expanded its applications in both clinical practice and experimental physiology [13, 17].

Chapter 3

Instruments and software

3.1 Spirometer

The respiratory flow signal was obtained using a custom-designed spirometer, which had been developed as part of earlier research conducted within the laboratory. It provides real-time visual feedback to guide the patient while performing the respiratory task, allowing the operator to monitor flow regularity and detect deviations from the target pattern. The device was designed with axial symmetry to measure airflow in both directions. A compact handheld grip facilitates user handling and stable positioning throughout the acquisition.

The spirometer operates on the Venturi principle, where airflow moving through a narrowed section of tubing creates a pressure difference that corresponds to the flow velocity. It consists of a circular Venturi tube with a total length of 14 cm. The outer diameter at both inlet and outlet is 3.2 cm, while the corresponding inner diameter is 2.5 cm. At the throat of the constriction, the internal diameter is 1.75 cm, producing a controlled acceleration of the air stream and a measurable pressure drop according to Bernoulli's law [19].

Two differential pressure sensors are connected to the main body of the tube through three ports placed along its longitudinal axis. The first port is located 2.5 cm from the inlet, with the remaining ports evenly distributed at intervals of 4.5 cm. This configuration allows for the identification of pressure gradients in both flow directions with minimal phase delay. Each end of the tube contains a metallic grid with circular holes of 2 mm in diameter to reduce turbulence and stabilize the flow estimation before it reaches the constriction. These grids extend 1 cm inside the tube and act as flow straighteners, improving the accuracy and repeatability of differential pressure measurements [19].

A detachable mouthpiece with an internal diameter of 2.8 cm is fixed to the proximal end of the tube, allowing for hygienic replacement between subjects. The spirometer itself measures a total length of 18 cm. The measured pressure difference between the two sensors is converted into flow using a calibrated transfer function obtained under controlled laboratory conditions. This resulting signal is then continuously acquired and synchronized with ultrasound imaging throughout the experimental procedure.

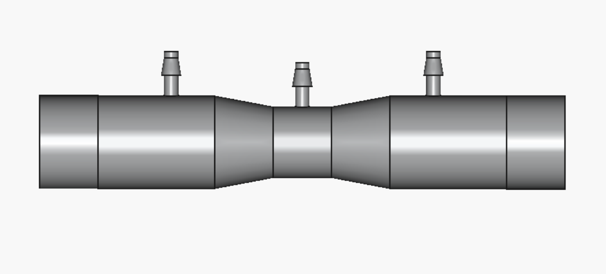

Figure 3.1: Spirometer: longitudinal view

Figure 3.2: Spirometer: transversal view

3.1.1 Mechanical airflow resistance

A mechanical airflow resistance was developed to evaluate the influence of controlled respiratory resistance on the pulsatility of the IVC. The device was designed to reproduce the standardized conditions of respiratory load during ultrasound acquisitions, ensuring repeatability of the condition. The respiratory load was designed using Autodesk Fusion 360 and 3D printed in PET plastic.

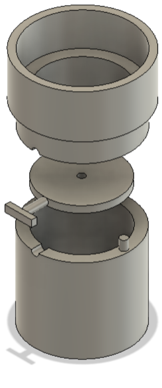

Figure 3.3: Airflow resistance design

The system consists of a cylindrical shell containing a rotating internal disk. The disk features a central hole of 1 mm in diameter, a size that provides a high level of airflow resistance while still allowing a minimal flow sufficient to keep the epiglottis open during the acquisition. This aspect is crucial because if the epiglottis closes completely, part of the air may remain trapped in the mouth or upper airways, preventing a true transmission of pressure changes to the thoracic cavity.
The mechanical design enables the operator to easily switch between two configurations by rotating the internal disk relative to the external body. This rotation system allows for quick modulation of airflow resistance without disconnecting the subject from the measurement setup, avoiding movement artefacts or repositioning errors.

- **Configuration A (no resistance)**: in this configuration the disk is aligned with the airflow path, leaving the channel fully open. This condition corresponds to spontaneous breathing, where the air passes freely through the device.

- **Configuration B (high resistance)**: the disk is rotated by 90° so that only the central hole remains aligned with the flow. The resulting restriction generates a significant increase in respiratory effort. This condition allows to investigate how increased intrathoracic pressure affects the IVC diameter and pulsatility.


(A)

(B)

Figure 3.4: Configurations of the airflow resistance: A) no resistance, B) high resistance.

The modular design of the resistance allows for future modifications, such as replacing the rotating disk with versions containing different hole diameters.

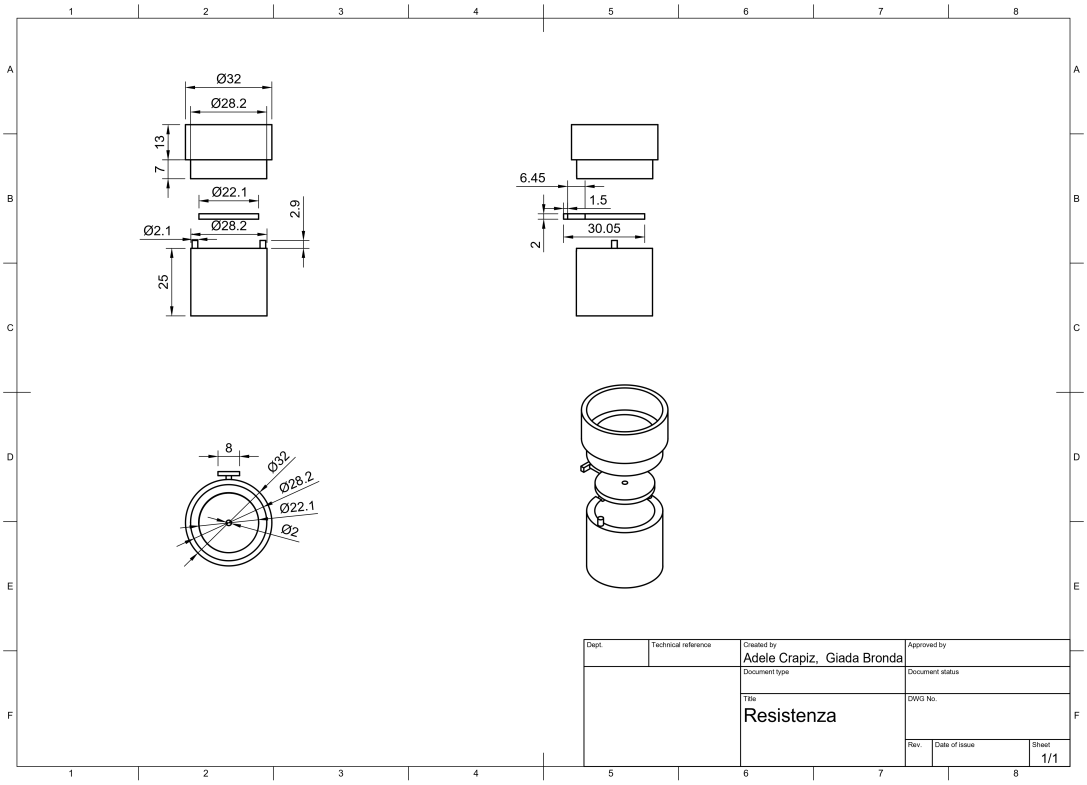

Figure 3.5: Airflow resistance orthogonal projection

3.1.2 Differential pressure sensors

The airflow signal is measured using two SDP816-125PA differential pressure sensors, designed by Sensirion AG, Switzerland. These sensors are designed to achieve high-resolution measurements of minor pressure differences and are suitable for respiratory and biomedical applications that require rapid dynamic response. Each sensor operates within a measurement range of ±125 Pa and provides an accuracy of ±3% of the measured value. The supply voltage ranges from 2.7 to 5.5 V, while the typical response time is below 5 ms. The internal digital resolution is 16 bits, and the device incorporates on-chip temperature compensation for operating conditions between −40°C and +80°C [20].

The output signal can be configured in two different modes: linear and square-root. In the linear configuration, the output voltage varies proportionally with pressure. However, this configuration is not fully symmetrical, as its dynamic range extends from -10% to +100% of the full scale span. In square-root mode, the output is fully bidirectional, with a stable zero reference and increased sensitivity at low differential pressures. This configuration is better suited for capturing inhalation and exhalation flows, especially in breathing patterns characterized by low flow rates or minimal pressure gradients [20].

The selected output configuration is the square root mode because it not only enables the accurate detection of airflow in both directions but also enhances sensitivity during the low-flow phases of the respiratory cycle. Moreover, it matches the non-linear relationship between pressure and velocity predicted by the Venturi effect, according to which air velocity increases as the cross-sectional area decreases and the corresponding pressure variation follows a quadratic rather than linear trend [19].

Figure 3.6: Pressure sensor

3.1.3 Data acquisition board

The pressure sensors are connected to a National Instruments USB-6001 data acquisition board (DAQ), a versatile USB-powered device commonly used for scientific and industrial measurements. This board provides eight single-ended analog input channels (AI), which can also be configured as four differential channels with an operating voltage range of ±10 V. This flexibility enables the simultaneous measurement of multiple sensors with different signal requirements, ensuring accurate and precise capture of both inspiratory and expiratory pressure signals [21].

It also provides two analog output channels (AO), with a voltage range of ±10 V, enabling the possibility to generate control signals for external devices. The device includes 13 digital input/output channels (DIO) and a 32-bit counter, facilitating the integration of timing signals and external sensors. The integrated analog-to-digital converter (ADC) on the board has a 14 bit resolution, providing highly accurate data conversion, and supports a maximum sampling rate of 20 kS/s. The absolute accuracy on full scale is 9.1 mV.

The DAQ is connected to a computer via USB, allowing real-time data acquisition and continuous monitoring of respiratory signals during experimental procedures. This real-time functionality is essential for evaluating respiratory dynamics and tracking the subject's breathing pattern throughout the experiment.

As mentioned above, two differential pressure sensors are used in this setup, and both are powered by a +5 V supply. A sensor is connected to the analog input channel 0 (AI0) to measure the pressure between the constriction and the outlet of the spirometer. The second sensor is connected to the analog input channel 1 (AI1) to measure the pressure between the constriction and the inlet, near the mouthpiece [21]. This configuration enables the precise recording of pressure differences between the two locations, allowing for an accurate calculation of airflow and respiratory parameters.

3.1.4 Signal processing

The output of the differential pressure sensors is a positive voltage signal, each corresponding to a differential pressure between two locations on the spirometer. Specifically, AI0 represents the pressure difference between the constriction and the outlet, while AI1 measures the difference between the constriction and the inlet. To convert raw voltage signals into differential pressure values, the square-root mode output is applied, with the pressure at the restriction being lower than at the inlet or outlet, resulting in negative pressure values [21].

Depending on the direction of airflow, the pressure difference varies. During inhalation, the pressure difference at the outlet (DPAI0) increases, resulting in a negative flow value. During exhalation, the pressure difference at the inlet (DPAI1) also increases, resulting in a positive flow. To correctly assign the flow direction, a sign function is used on the pressure differences, which ensures an accurate classification of the flow direction for both phases of respiration [14].

Additional measures are put in place to reduce errors during the shift between inhalation and exhalation, as this transition can result in positive spikes. The signal is classified as exhalation when DPAI0 is greater and positive and as inhalation when DPAI1 is greater and positive. These rules help prevent incorrect transitions during low-phases, where pressure changes are typically more gradual [17].

Pressure signals are filtered using a second-order Butterworth low-pass filter, which ensures effective noise reduction without introducing significant phase distortion. The cut-off frequency is set to 2 Hz, which balances the need for smooth signal processing while preserving the accuracy of respiratory measurements. Filtering is applied in blocks of 100 samples to allow real-time data processing. An IIR filter is used to balance signal quality and processing delay, as an FIR filter would introduce higher latency.

Once filtered, the two differential pressure signals (DPAI0 and DPAI1) are combined to obtain a continuous flow signal. During exhalation, the AI0-based signal is used, while the AI1-based signal is used during inhalation. The flow calculation is based on theoretical assumptions of the continuity equation and Bernoulli's principle, which assume that the fluid (air) is incompressible and ideal. Since air is compressible and pressure losses due to friction and airway geometry are not considered, the computed flow results are an approximation.

3.2 Ultrasound system

The ultrasound system was employed to acquire real-time B-mode images of the inferior vena cava during the respiratory maneuvers. The following subsections describe the main components of the system, including the ultrasound scanner, the probe, and the software used for image acquisition and analysis.

Figure 3.7: Ultrasound system

3.2.1 Ultrasound scanner

For the acquisition of IVC ultrasound data, a portable ultrasound scanner, the MicrUs EXT-1H, developed by Telemed Ultrasound, was used. The device is powered directly via a USB connection to a computer, which allows it to operate as a compact and lightweight diagnostic platform suitable for both laboratory and point-of-care applications. Its plug-and-play configurations enable fast setup and data transfer, making it suitable for experimental protocols requiring synchronized multimodal acquisition [22].

The MicrUs EXT-1H is compatible with a broad range of transducers, including linear, convex, micro-convex, and endocavitary probes, thus supporting a wide spectrum of clinical and research applications. The system operates with a multi-frequency probe ranging from 2 to 15 MHz, which allows optimization of both penetration depth and spatial resolution according to the anatomical region of interest. As a result, high-quality imaging of deeper abdominal structures, like the IVC, can be obtained while preserving the high frame rates essential for dynamic assessment [23].

The scanner provides standard imaging modalities, like B-mode (brightness mode) and M-mode (motion mode). B-mode produces two-dimensional grayscale images that enable the assessment of vessel geometry and wall motion. In contrast, M-mode allows the evaluation of temporal changes along a single scan line, which is essential for investigating cyclic phenomena, such as the collapsibility and pulsatility of the IVC.

The ultrasound images are displayed in 256-tone greyscale and can be exported in multiple formats, including AVI, BMP, TIFF, and DICOM, ensuring compatibility with post-processing and quantitative analysis tools. The standard hardware packaging includes the MicrUs EXT-1H beamformer base unit, a USB connection cable, installation software, user documentation, and the selected ultrasound transducers [22].

3.2.2 Ultrasound probe

A C5-2R60S-3 convex probe, manufactured by Telemed, was used to acquire IVC images. This transducer operates within a frequency range of 2.0-5.0 MHz and provides a 60°field of view, parameters that offer an optimal balance between penetration depth and spatial resolution. This setup provides a clear visualization of the deep vascular structures in the abdomen, including the IVC and its connection to the right atrium [22].

Convex or curvilinear probes in the 2-5 MHz frequency range are used in point-of-care and abdominal ultrasound, as their wide footprint and field of view allow visualization of deep organs and large vessels within a single frame [24]. The lower frequency allows sound waves to penetrate deeper into soft tissues while ensuring sufficient lateral resolution for a precise assessment of vessel diameter and wall movement. This setup also supports the identification of anatomical structures such as the hepatic veins and diaphragm, which play a crucial role in the precise localization of IVC and proper alignment of the probe.

3.2.3 Software EchoWave II

The ultrasound scanner utilized EchoWave II, a software developed by Telemed for real-time image control, acquisition, and management. The software interface is designed for visualize ultrasound images and videos in B-mode or M-mode. The acquired data can be stored in different formats, such as AVI, BMP, TIFF, and DICOM, for post-processing [22].

EchoWave II enables optimization of imaging parameters according to the subject's anatomical characteristics to optimize visualization. These include scan depth, which defines how deep the ultrasound beam penetrates the tissue, the focus position which determines the region of maximum lateral resolution; gain is the amplification of the ultrasound signals to adjust the overall brightness of the image. The dynamic range controls the contrast between bright and dark regions and affects how the interface between tissues is visualized. The acoustic power regulates the transmitted energy influencing the intensity of the signal. The software also provides manual control of time gain compensation (TGC), which allows adjustments of brightness at different depths. Finally, the ultrasound frequency can be selected to balance spatial resolution and penetration depth.

The software also includes additional image enhancement tools to improve spatial and temporal image quality. These include speckle reduction and frame averaging algorithms that mitigate the granular texture and view smoother ultrasound images. Rejection filters, which are used to suppress background noise.

The use of EchoWave II allowed precise adjustments of acquisition parameters for each subject, ensuring optimal visualization of the IVC walls and uniform image quality across recordings and generated images suitable for an accurate processing.

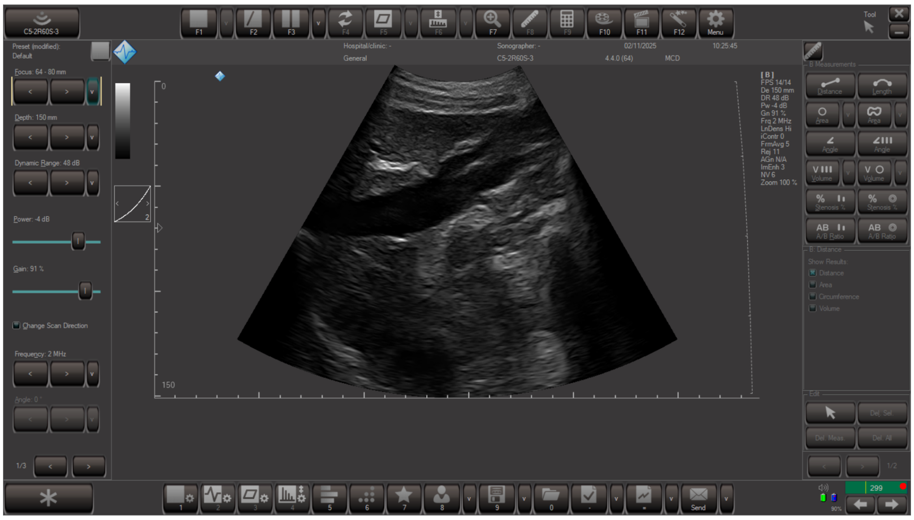

Figure 3.8: EchoWaveII interface

3.2.4 VIPER

VIPER is a software platform developed by VIPER S.r.l. for the semi-automatic analysis of B-mode ultrasound videos of blood vessels. It applies an edge-detection algorithm to track the diameter of the vessel in frames in both longitudinal and transverse views [2].

In transverse mode, the user manually identifies the center of the vessel in the first frame, after which the algorithm automatically segments and tracks the contour of the vessel through subsequent frames. In longitudinal mode, the operator first defines the main axis of the vessel by selecting two points along its path, and then specifies the start and end positions of the segment to be analyzed. The software extracts the walls of the vessel and calculates the time-dependent diameter, generating a continuous waveform that reflects the dynamic changes in vascular dimension during acquisition [13].

The resulting diameter time series can be exported for further quantitative processing, including spectral analysis and synchronization with physiological signals. By automating contour detection, VIPER reduces operator dependency and enhances measurement reproducibility by enabling standardized diameter extraction.

Two operating modes are available within the VIPER framework:

- **Offline mode**: this setup enables the post-processing of recorded ultrasound videos for retrospective analysis of vessel behaviour. Provides advanced filtering, artifact correction, and synchronization with external biosignals, supporting a comprehensive assessment of cardiovascular and respiratory effects.

- **Real-time mode**: this setup facilitates the tracking of vessels in real-time during ultrasound data acquisition. It uses a lightweight, GPU-optimized version of the tracking algorithm to provide immediate visualization of vessel diameter variations.

Real-time processing enables the ongoing evaluation of hemodynamic parameters, making it suitable for clinical monitoring applications.

The resulting analysis produces a segmented video showing the detected vessel walls over time, and an Excel file containing quantitative data. The output file includes the temporal evolution of the IVC diameter as well as respiratory and cardiac components obtained from signal decomposition. To providean overview of the vessel's general characteristics, the software also computes and saves morphological and dynamic parameters including the mean,maximum and minimum diameters, as well as indices that describe the vessel pulsatility: Caval Index (CI), Respiratory Caval Index (RCI) and Cardiac Caval Index(CCI).

These outputs allow a comprehensive quantitative evaluation of vessel compliance and hemodynamic variability, providing standardized and reproducible parameters for both experimental and clinical investigations.

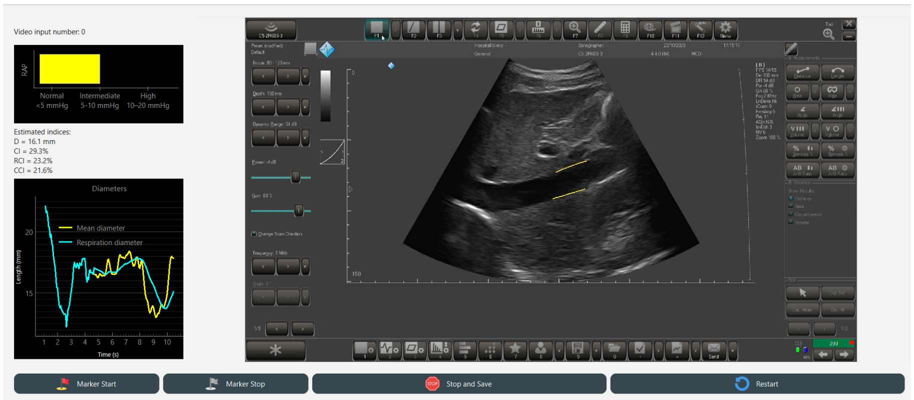

Video input number: 0

Estimated indices:
D = 16.1 mm
CI = 29.3%
RCI = 23.2%
CCI = 21.6%

Figure 3.9: VIPER real-time mode

Chapter 4

Experimental Evaluation

This chapter describes the experimental and numerical procedures carried out to evaluate the reliability of inferior vena cava (IVC) measurements under a controlled respiratory condition. This work focuses on one specific condition designed to provide consistent and physiologically relevant variations in intrathoracic pressure. Ultrasound and spirometry signals were acquired simultaneously and then processed to extract the IVC diameter over time. Using these data, key parameters such as the Caval Index (CI) and the variation of the mean diameter were computed. The chapter outlines the acquisition protocol, the signal elaboration steps, and the validation strategies adopted to ensure the robustness of the results. This focused approach aims to assess whether a simplified, standardized breathing maneuver can improve the repeatability and clinical utility of IVC ultrasonography.

4.1 Experimental protocol

The study aimed to standardize the respiratory pattern to obtain a more accurate ultrasound evaluation of the IVC. The proposed protocol was designed to perform non-invasive, repeatable, and easy-to-perform measurements.

4.1.1 Preliminary pilot tests

Preliminary pilot tests were carried out to explore the IVC response under different breathing conditions. Several breathing patterns were explored, including sinusoidal and square-wave profiles, as well as different amplitudes such as light, medium, and deep breathing. Other trials focused on single-phase maneuvers, involving inspiration or expiration only, and on standardized full breathing cycles. Moreover, different levels of respiratory resistance were tested using a previous design that allowed adjustments of the overlap between the internal and external disks of the mechanical airflow resistance.

The preliminary analysis allowed made it possible to identify the condition that produced a consistent reduction in IVC diameter after the introduction of respiratory resistance, a response that is comparable to the one observed during the clinically adopted sniff test. This specific inspiratory condition was selected because it combines physiological relevance (comparable to the clinical sniff maneuver) with repeatability and ease of execution, allowing a controlled yet natural modulation of intrathoracic pressure.

4.1.2 Experimental conditions

The analysis focused on evaluating the diameter of the IVC and its collapsibility during a brief inspiratory maneuver performed with the application of a mechanical respiratory load. During each trial, the subject inhaled through the spirometer while a simultaneous ultrasound recording of the IVC was acquired. Measurements were collected in both the supine (normal) position and during passive leg raising (PLR), the latter included to perform a preliminary assessment of the robustness and consistency of the proposed approach.

4.1.3 Acquisition Protocol

The total duration of each acquisition was 6 seconds and consisted of inspiration performed at a constant target flow. During the first 3 seconds, subjects inhaled without resistance; at the third second, the mechanical resistance was introduced by rotating the internal disk of the respiratory load to reach configuration B (Figure 3.4), corresponding to the high-resistance setting. The patients continued inhaling for an additional 3 seconds while maintaining the same flow rate.

The target flow value was obtained through pilot tests performed at different flow levels to identify a value that could be achieved by all subjects while still inducing measurable variability in the IVC diameter. The selected target was -0,45 L/s, where the negative sign reflects the convention adopted for the flow of inspiration.

The acquisition was repeated in both the normal and PLR positions. For the PLR condition, the subject was asked to elevate the legs to a 45° angle. To allow the venous return to stabilize, a waiting period of approximately three minutes was observed before performing the inspiratory maneuver. For each condition (Normal and PLR), three trials were acquired and later averaged to reduce intra-subject variability.

The study was conducted on seven healthy subjects ($n = 5$ females and $n = 2$ males; age 25.7 ± 1.6 years).

4.1.4 Experimental setup

The experimental setup consisted of a clinical bed on which each subject lied in a supine position to facilitate abdominal ultrasound imaging. The ultrasound probe was positioned, as suggested by clinical indications, approximately 2cm below the xiphoid process in the longitudinal configuration, with the orientation marker directed towards the subject's cranium. This setup enabled the visualization of the IVC along the intrahepatic tract up to its junction with the right atrium, ensuring consistent probe alignment.

The acoustic coupling was optimized using a standard ultrasound gel to prevent air interface artifacts. The operator maintained a light pressure to prevent partial vessel compression. To ensure reproducibility of the IVC diameter measurements, the same probe position was maintained across all recordings for each subject

The acquisition of the ultrasound images was managed through EchoWave II software. The ultrasound frequency was fixed at 2 MHz to guarantee a good balance between depth penetration and spatial resolution for the visualization of the IVC. Other parameters - gain, acoustic power, depth and focus position- were adjusted differently for each subject based on the anatomical characteristics to enhance the vessel visibility. Once the parameters were set, they were kept constant throughout the whole acquisition.

Three computers were used simultaneously: one to manage the spirometric acquisition and processing, a second to control the ultrasound device via EchoWave II software, and a third to run VIPER in real time for vessel segmentation and diameter tracking. The live feed of EchoWave II was captured and displayed to VIPER through a frame grabber and an HDMI cable that linked the two computers. To ensure temporal synchronization between spirometry and ultrasound recordings, a manual flag was inserted in the VIPER software at the start of each spirometric acquisition.

The spirometer was interfaced to a computer through a DAQ board and a MATLAB script was developed to display, on the same graph, the respiratory airflow in real time and a reference line representing the target airflow. The live visualization guided the subjects through the test, helping them to maintain the inspiration at a constant flow throughout the manoeuvrer. During each acquisition the script automatically saved the recorded pressure signals, the raw and filtered flow signal along with the corresponding temporal vector. Some metadata such as the subject ID, type of acquisition and sample frequency were saved as well. This configuration allowed synchronized and efficient data collection, visualization, and processing during the recording session.

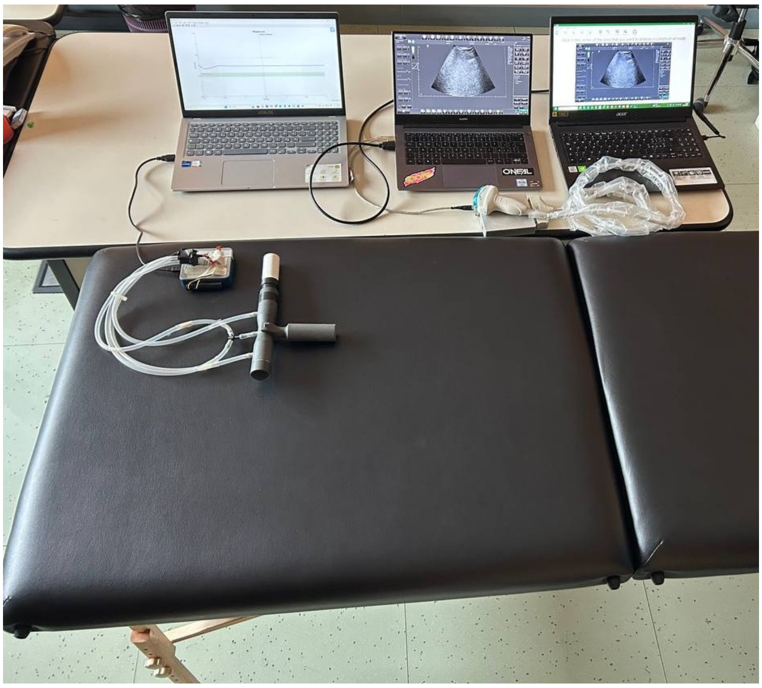

Figure 4.1: Experimental setup

4.1.5 Spirometry acquisition System

A specific MATLAB interface was developed to ensure standardized and synchronized acquisition of inspiratory flow signals under both normal breathing and passive leg raising (PLR) conditions. At the beginning of each session, the operator selected the subject directory through a dialog window and specified the experimental condition (`0 = Normal`, `1 = PLR`).

The system was connected to a National Instruments DAQ (USB-6001) configured with two analog voltage inputs (`Dev1/AI0` and `Dev1/AI1`) connected to the spirometer's differential pressure sensors. Each acquisition lasted 6 s and was divided into two equal phases: 0–3 s of free inspiration and 3–6 s of inspiration against the mechanical resistance. This fixed duration enables direct temporal alignment with ultrasound recordings.

A custom graphical interface provided continuous visual feedback of the instantaneous flow signal, displaying in real time the measured trace, a dashed line indicating the target inspiratory flow, and a shaded horizontal band representing the tolerance range. A vertical reference line marked the onset of resistance, and a brief 5 s countdown preceded each trial to facilitate subject preparation and synchronization.

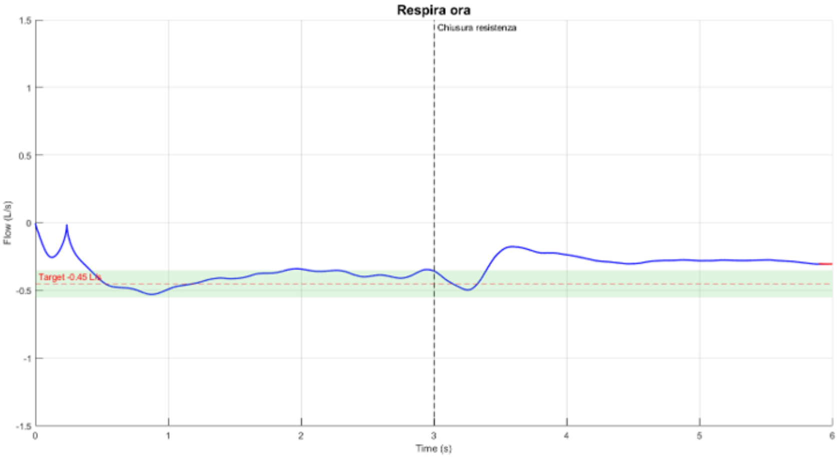

Figure 4.2: Spirometry acquisition system

Analog voltages from the sensors were converted into differential pressure values using their factory square-root transfer function (5 V supply), which compensates for the nonlinear sensor response. The conversion was expressed as:

$$p = \operatorname{sign}\left(\frac{V}{V_{DD}} - 0.5\right)\left(\frac{V}{0.4\,V_{DD}} - 1.25\right)^2 \times 133 \quad [\mathrm{Pa}]$$

The resulting pressure signals were then filtered using a second-order Butterworth low-pass filter at 2 Hz to remove high-frequency noise while preserving respiratory dynamics. Flow was computed from the filtered pressure at channel `AI0` according to Bernoulli's relation for a Venturi geometry:

$$Q = -A_2\sqrt{\frac{2|p|}{\rho_{\mathrm{air}}\left(1-(A_2/A_1)^2\right)}} \quad [\mathrm{m}^3/\mathrm{s}]$$

and converted to [L/s] by multiplying by 10^3. The negative sign reflects the inspiratory phase. The model parameters included $\rho_{\mathrm{air}} = 1.164\,\mathrm{kg/m^3}$, $r_1 = 12.5\,\mathrm{mm}$, $r_2 = 8.75\,\mathrm{mm}$, with $A_1 = \pi r_1^2$ and $A_2 = \pi r_2^2$. The target inspiratory flow was set to $Q_{\mathrm{target}} = -0.45$ L/s with a tolerance of ± 0.10 L/s.

During acquisition, both the raw flow and a smoothed trace (250 ms moving-average window) were displayed in real-time. At the end of each recording, the script automatically computed the mean and standard deviation of the smoothed flow for both phases. Timestamps marking the start, end, and total acquisition duration were also saved for synchronization purposes.

All data were automatically stored in a single `.mat` file containing the raw and filtered pressure signals, computed and smoothed flow traces, temporal information, phase segmentation, and summary statistics of flow and pressure, together with metadata describing the subject and experimental condition.

This interface enabled controlled and repeatable inspiratory maneuvers, providing synchronized respiratory data with a temporal structure compatible with the ultrasound acquisition and subsequent quantitative analysis.

Chapter 5

Data processing

All data were processed using custom MATLAB scripts developed to preprocess the ultrasound Excel files obtained from Viper, align the diameter signal with the spirometric recordings, extract relevant quantitative parameters, and perform both intra- and inter-subject statistical analysis.

5.1 Signal segmentation and preprocessing

The first step concerns the segmentation of the diameter time series obtained from the Viper software. Each Excel file contained three main columns that were taken into account: the time vector, the raw diameter signal, and a marker column. The marker is a Boolean parameter that switches from 0 to 1 when the spirometric acquisition starts, allowing synchronization between the signals.

The segmentation, implemented in the custom MATLAB script, automatically detected the first occurrence at which the marker switched to 1 and stored the corresponding time instant. From then on, a 6-second window of the diameter signal was extracted, which corresponds to the duration of the spirometric recording.

Within the 6 second window, the signal was further divided into two consecutive segments: the first three seconds, corresponding to unresisted inspiration (pre-resistance phase), and the last three seconds, corresponding to inspiration performed against the respiratory load (post-resistance phase).

Each processed acquisition was saved as a structured `.mat` file containing the segmented diameter series, the associated time vector, and basic metadata describing the subject, posture, and trial. For quality control, the script produced plots showing the complete 0-6 s trace with the resistance insertion highlighted, allowing visual inspection of the segmentation.

5.2 Integration with spirometry and computation of quantitative indices

The second processing stage aimed to integrate the IVC diameter signals with the corresponding spirometric acquisitions and to compute quantitative indices describing the respiratory-induced variations of the vessel. The implemented MATLAB script automatically handled two input directories: one containing the `.mat` files of the segmented IVC diameter signals and another containing the spirometric recordings. The user was asked to select the folders through dialog windows, after which the program created an output directory to store the elaborated data and figures. Each file was named following a standardized format that included the subject identifier, posture (NORMAL or PLR), and trial number, ensuring automatic pairing between the two data sources.

For each acquisition, the program extracted the segmented diameter signal, its time vector, and the inspiratory flow signal from the corresponding `.mat` files. The temporal alignment between ultrasound and spirometry was maintained through the acquisition timestamps stored during recording.

To quantify the mechanical response of the IVC during the two phases (0–3 s unresisted, and 3–6 s resisted), several parameters were calculated for each segment: the mean diameter (D_{mean}), representing the average vessel size; the maximum and minimum diameters (D_{max} and D_{min}), corresponding to the greatest collapse and distension of the IVC; and the absolute diameter variation ($\Delta D = D_{\text{max}} - D_{\text{min}}$). To evaluate the IVC collapsibility and indirectly assess the intravascular volume status, the Caval Index (CI) was computed as:

$$CI = \frac{D_{\text{max}} - D_{\text{min}}}{D_{\text{max}}} \times 100$$

For each trial, the script also calculated the change in mean diameter between the two phases ($\Delta D_{\text{mean}} = D_{\text{post,mean}} - D_{\text{pre,mean}}$) and stored all computed metrics in a summary table. This table contained, for each subject and trial, posture, condition, and all quantitative parameters derived.

The same data structure was used to generate graphical outputs. Two main types of plots were automatically produced:

- **Bar charts** showing the variation of the IVC diameter (ΔD) and the CI under the two postures, enabling an immediate visual comparison.

- **Time-series panels** displaying the synchronized traces of IVC diameter and inspiratory flow over the 0–6 s interval. Each panel included grey curves representing individual trials and a bold black line corresponding to their average. A vertical reference line at 3 s marked the insertion of the resistance, allowing the temporal correlation between respiratory effort and venous deformation.

5.3 Statistical analysis

The statistical analysis performed in this work was based on inferential methods used to assess differences in physiological measurements within subjects and between different conditions. Inferential statistical analysis infers properties of a population by testing hypotheses and obtaining estimations. The considered hypotheses are the null hypothesis (H_0) that represents the absence of an effect or difference between conditions, and the alterative hypothesis (H_1) which assumes a significant effect. The hypothesis testing allows to decide whether to accept or reject the predefined null hypothesis based on a chosen significance level (α) usually set at 0.05, represents the probability of committing a 5% error by incorrectly rejecting the null hypothesis that is, by concluding that an effect exists when it actually does not [25].

5.3.1 Parametric and non-parametric tests

Statistic tests can be divided into parametric and non parametric tests. The first rely on assumptions about the shape and parameters of the population distribution from which the data was collected. These are typically used for continuous data and are considered more powerful, meaning they can be more likely to detect a real effect. The Student's t-test is a parametric test that evaluates whether the means of two related samples differ significantly. It compares the mean difference to the variability between the data and produces a p-value that quantifies the probability of observing a difference by chance.

Non parametric tests do not require assumptions about the population distribution. They are characterized by a lower power but are more appropriate for small samples. The Wilcoxon signed-rank test is used to compare two related samples and operates on the ranks of the absolute differences between paired observations. Each difference is assigned a rank according to its magnitude and the signs indicate the direction of change. The sums of the positive and negative ranks are calculated and used to compute then test statistic T, which is the smaller of the two sums. This number reflects how balanced the positive and negative differences are. If most differences are positive or all negative, T will be small, evidence that the median difference is not zero. Otherwise no real difference will be detected.

5.3.2 Implementation of the analysis

Statistical analysis was performed using a custom MATLAB script designed to process the summary tables generated in the previous steps of data processing. The goal of this stage was to evaluate whether posture (NORMAL vs. PLR) induced statistically significant differences in the mean diameter variation (ΔD_{mean}) and in the mean CI (CI_{mean}) and to assess the consistency of their modulation throughout subjects.

The script automatically imported the summary file and verified the presence of the required variables. The two postural conditions were identified as separate experimental groups for comparison. Three main analyses were conducted:

- One-sample tests to assess whether the mean diameter variation within each posture differed significantly from zero
- Paired comparisons between postures for both ΔD_{mean} and CI_{mean}
- Computation of descriptive statistics and effect sizes (Cohen's d_z).

For the one-sample analysis, both parametric and non-parametric tests were applied to ΔD_{mean} values within each posture. Specifically, a Student's t-test and Wilcoxon signed-rank test were performed to test the null hypothesis of zero mean variation. For each group, the mean, standard deviation, median, and interquartile range were calculated, together with Cohen's d_z effect size. These metrics allowed the assessment of the overall direction and magnitude of the IVC diameter variations induced by respiratory load.

A paired comparison was conducted between the two postural conditions (NORMAL and PLR) for both ΔD_{mean} and CI_{mean}. Each subject contributed a pair of values (one for each posture), enabling within-subject evaluation while minimizing inter-subject variability. Both paired t-tests and Wilcoxon signed-rank tests were conducted. For each comparison, the mean and standard deviation of the paired differences, effect size (d_z), and the corresponding p-values are provided. These analyses aimed to verify whether postural change significantly affected IVC collapsibility and mean diameter variation.

The script automatically compiled the resulting statistics into two structured tables:

- **OneSample_DeltaD:** containing one-smaple test results for ΔD_{mean} in each posture
- **Paired_Comparison:** summarizing paired results for ΔD_{mean} and CI_{mean} between NORMAL and PLR postures, together with effect size and significance levels.

All results were automatically exported to both an Excel report and a MATLAB structure file.

This statistical workflow provided a robust framework for validating the physiological findings obtained in the previous sections. By combining paired and one-sample statistical tests, the analysis enabled a quantitative evaluation of the influence of respiratory resistance and posture on IVC dynamics, highlighting consistent trends across subjects and conditions.

The detailed results of the statistical tests are reported in Chapter 5, where they are discussed in relation to the numerical outcomes.

Chapter 6

Numerical results

The quantitative analysis examined the impact of the inspiratory resistance on the diameter of the IVC during controlled inspiration. The aim is to quantify how mechanical load during inhalation alters the IVC dynamics and dimension, aspects that influence the venous return. Each trial was divided into two sections: a pre-resistance phase, corresponding to spontaneous inhalation, and a post-resistance phase, in which a mechanical load was introduced by rotating the disk of the designed resistance. This approach enabled the isolation of the effects of inspiratory resistance while maintaining a constant flow rate throughout the manoeuvre. As a result, any observed variation in IVC diameter can be attributed to changes in inspiratory load, rather than differences in respiratory effort or airflow.

In spontaneous breathing, the inspiratory decrease in intrathoracic pressure slightly facilitates venous return, producing a moderate and physiological narrowing of the IVC. When resistance is applied, the subject must generate a larger negative intrathoracic pressure to maintain the same inspiratory flow. This stronger pressure gradient between the thoracic and abdominal cavities enhances the mechanical stress acting on the IVC wall, leading to a more pronounced and visible collapse.

6.1 Effect of Inspiratory Resistance in Supine Posture

6.1.1 Variation of IVC Diameter

Figure 6.1 illustrates the comparison of the diameter variation (ΔD) between pre and post resistance phases for each subject. Across all subjects, ΔD assumes negative values, indicating a reproducible decrease in IVC diameter when the resistance is introduced. This reduction can be explained by the increase in intrathoracic pressure generated by the mechanical load. When the subject keeps inhaling against resistance without altering the airflow rate, the intrathoracic pressure rises and temporarily reduces venous return to the right atrium and enhances the IVC collapse.

The observed ΔD values vary between subjects, which is expected due to physiological variability in compliance, venous tone,muscle engagement and effort. Despite the inter-individual differences, the overall trend is consistent in all trials. This consistency supports the reliability of the proposed experimental protocol in inducing a measurable haemodynamic perturbation. It also supports the use of mechanical resistance as a tool to explore the coupling between respiratory pressure variations and venous return dynamics.

This result demonstrates that even without a full respiratory cycle, the controlled inspiratory phase on its own is sufficient to detect significant variations in venous return dynamics. The applied mechanical load serves as a perturbation that reveals the coupling between airway pressure and the behaviour of the IVC.

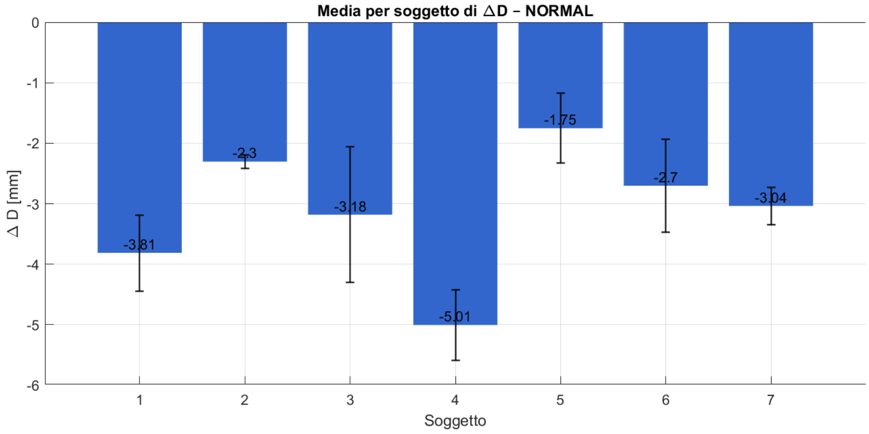

Figure 6.1: Bar plot of variation of IVC diameter for each subject

6.1.2 Minimum IVC Diameter

The minimum diameter $D_{\min}$ represents the maximal inspiratory collapse of the vein and is an indicator of venous return efficiency and right atrial filling during inspiration. This parameter provides insight into the dynamic relationship between intrathoracic pressure changes and central venous volume. Figure 6.2 compares the minimum IVC diameter before and after applying inspiratory resistance in the supine posture.

The $D_{\min}$ reduction, just like ΔD values, vary among individuals depending on their anatomy and physiological functionalities. Subjects with a more distended IVC or higher CVP tend to show smaller changes, while those with a compliant venous system exhibit greater collapsibility.

A consistent reduction in $D_{\min}$ is observed in all subjects after the introduction of the inspiratory load. This result reflects the physiological enhanced collapse of the vein due to the increased intrathoracic pressure that opposes to venous return.

The smaller post-resistance $D_{\min}$ indicates a higher dynamic compliance,meaning that the vein is more sensitive to pressure variations. A larger value, after resistance, would indicate that the vein remained more distended throughout the inspiration, suggesting reduced collapsibility and a lower sensitivity to pressure variations, typically associated with higher CVP or augmented preload.

By analysing D_{min}, it is therefore possible to quantify the vessel's compliance and its responsiveness to mechanical changes in intrathoracic pressure. The consistent reduction in D_{min} observed after resistance confirms that the manoeuvre increased the inspiratory load, enhancing the mechanical modulation of venous return in a controlled and reproducible manner.

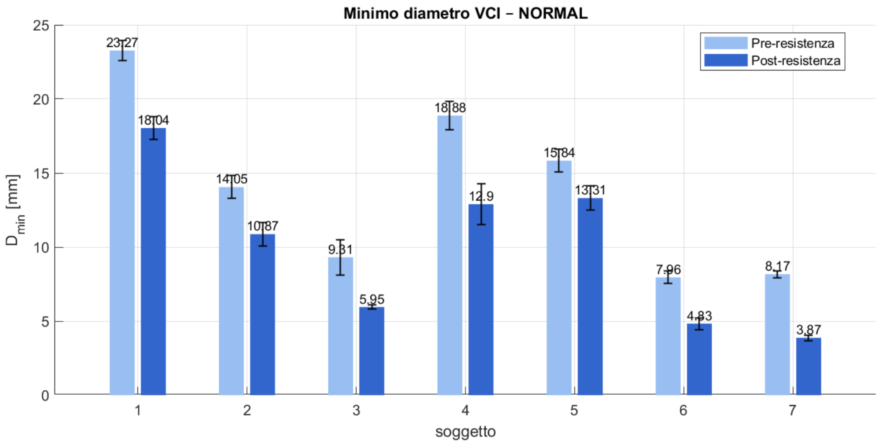

Figure 6.2: Bar plot of the minimum IVC diameter

6.1.3 Inspiration-only Caval Index

To evaluate the dynamic modulation of the IVC, the Caval Index was calculated. When inspiratory resistance is applied, the increase in intrathoracic pressure enhances the mechanical stress on the vessel wall, amplifying the venous collapse and thus increasing the CI. This result shows that the respiratory load increases the oscillations of the venous lumen, making the respiratory modulation easier to detect and quantify through ultrasound analysis of the IVC.

As shown in Figure 6.3, in the NORMAL posture, applying the respiratory load increases intrathoracic pressure during inspiration and increases the compressive forces on the IVC. As a result, the inspiration-only CI increases post-resistance, indicating greater collapsibility. Because this CI is calculated within inspiration only, it reflects dynamic compliance and preload sensitivity during the most pressure-sensitive phase.

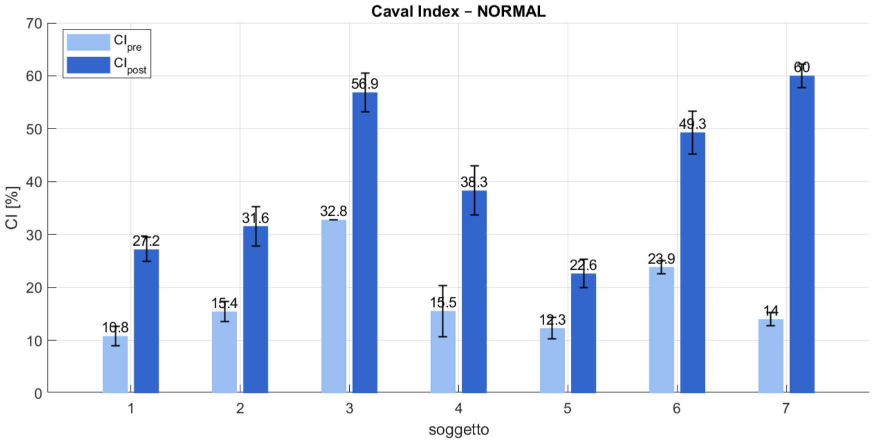

Figure 6.3: Bar plot of Inspiration-only CI

6.2 Comparison Between Postures

To further investigate the influence of preload on venous dynamics, a comparative analysis was conducted between supine (NORMAL) and passive leg raising (PLR) conditions. The parameters defined above (ΔD, $D_{\text{min pre}}$, $D_{\text{min post}}$, CI_{pre}, and CI_{post}) were evaluated across postures to determine how changes in venous return influence the effects of inspiratory resistance. In addition, a global Caval Index (CI_{pct}) was calculated throughout the inspiratory window to provide an overall measure of venous variability during the complete maneuver.

6.2.1 Minimum IVC Diameter and Variation of Diameter across Posture

Figure 6.4 and Figure 6.5 show the comparison of $D_{\text{min post}}$ and ΔD between the NORMAL and PLR conditions. In both postures, the introduction of inspiratory resistance results in a decrease in the minimum diameter and in negative ΔD values, demonstrating the consistent physiological effect of the load. However, the magnitude of this reduction is smaller in the PLR posture.

This attenuation reflects the preload increase induced by leg elevation, which raises central venous pressure and partially offsets the collapse generated by intrathoracic pressure during resisted inspiration. While the direction of the response remains consistent across both postures (diameter reduction post-resistance), the amplitude of the effect depends on the baseline venous filling. These behaviours support the hypothesis that inspiratory resistance acts mainly through modulation of preload and venous compliance.

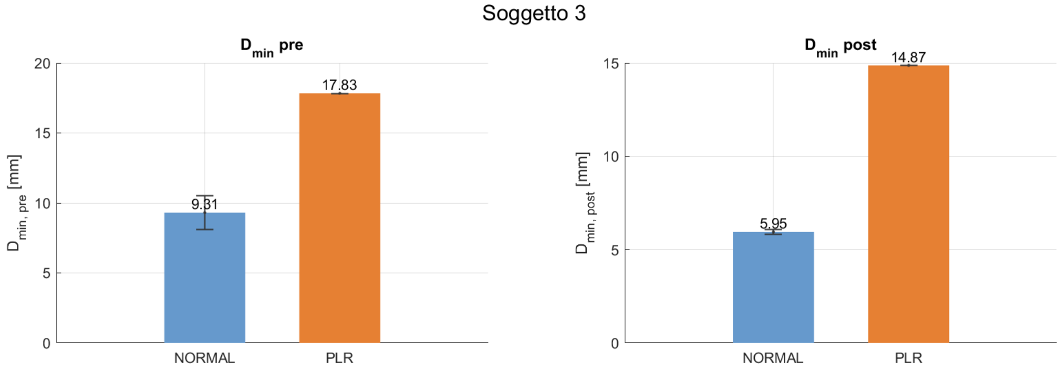

Figure 6.4: Bar plot of minimum diameter of IVC in normal and PLR postures

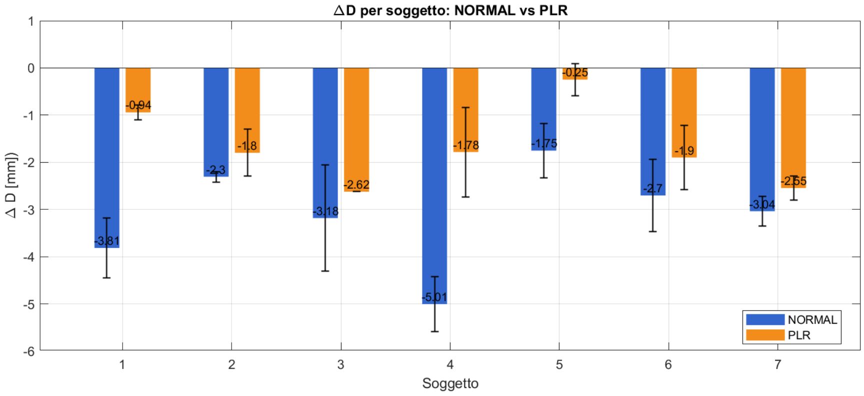

Figure 6.5: Bar plot of variation of diameter of IVC in normal and PLR postures

6.2.2 Inspiration-Only CI and Global CI

As shown in Figure 6.6 and Figure 6.7, the behaviour of both inspiration-only CI and CI_{pct} mirror the trends observed in $D_{\text{min post}}$ and ΔD.

In the supine posture, the CI increases evidently after resistance, indicating that the IVC becomes more dynamically compliant and exhibits larger diameter oscillations within the inspiratory phase. In the PLR posture, the CI also tends to increase post-resistance; the magnitude of this change is smaller, confirming that the elevated preload reduces the relative collapsibility of the vein.

The global CI_{pct} calculated over the entire inspiratory segment provides complementary evidence: while both postures show an overall increase in cyclic variation with resistance, the effect is attenuated in PLR. These findings highlight that although the resistance consistently amplifies IVC modulation, the degree of modulation is significantly influenced by preload conditions.

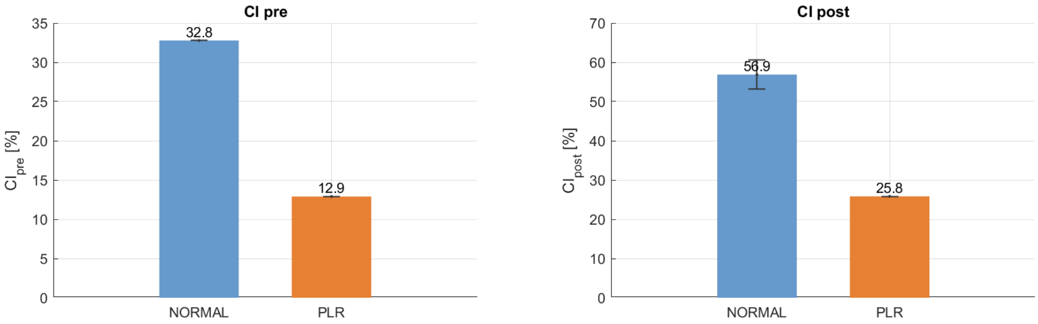

Figure 6.6: Bar plot of inspiration-only CI in normal and PLR postures

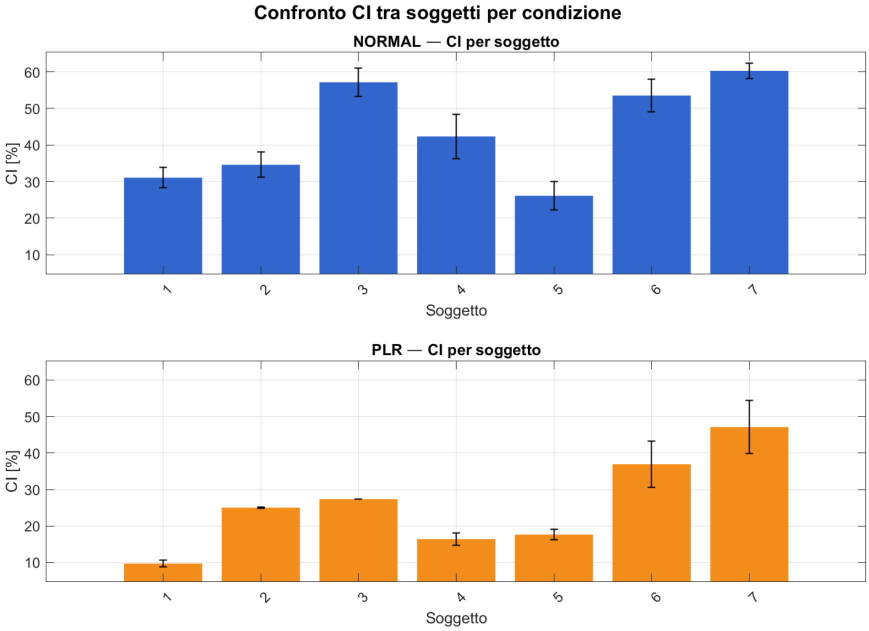

Figure 6.7: Bar plot of global CI in normal and PLR postures

6.3 Statistical results

To validate the observations described in the previous sections, a dedicated MATLAB script was employed to perform the statistical analysis on the parameters extracted from all subjects and postures. The analysis aimed to determine whether the effects of inspiratory resistance and posture (NORMAL compared with PLR) on the inferior vena cava (IVC) diameter and collapsibility were statistically significant. Three primary parameters were considered: the mean variation of the IVC diameter (ΔD_{mean}), representing the change in mean diameter between the pre- and post-resistance phases; the minimum diameter (D_{min}); and the mean Caval Index (CI_{mean}), quantifying the collapsibility of the vessel.

6.3.1 Testing strategy

Normality of the data distributions was assessed prior to hypothesis testing. Parametric tests (Student's t-test) were applied when the normality assumption was satisfied, whereas non-parametric tests (Wilcoxon signed-rank test) were used otherwise. All tests were two-sided with a significance threshold of $\alpha = 0.05$. For each analysis, both the p-value and the standardized effect size (Cohen's d_z) were reported to describe the strength of the observed differences.

6.3.2 Pre- and post-resistance comparison

A paired analysis was performed across all acquisitions to quantify the direct effect of the inspiratory load on IVC dynamics. The comparison relied on within-acquisition differences (POST–PRE) for ΔD_{mean}, D_{min}, and CI_{mean}, providing a direct measure of how inspiratory resistance modulated each parameter. Descriptive statistics, effect sizes, and two-sided hypothesis tests are summarized in Table 6.1.

Variable	$n_{\textbf{pairs}}$	**Mean Diff**	$\textbf{SD}_{\textbf{diff}}$	d_z	p **(t)**	p **(W)**	**95%** $\textbf{CI}_{\textbf{mean}}$
ΔD_{mean} (POST–PRE) [mm]	48	−2.16	1.67	−1.30	9.33×10^{-12}	3.06×10^{-11}	[−2.64, −1.67]
D_{min} (POST–PRE) [mm]	48	−2.85	2.06	−1.38	1.23×10^{-12}	7.10×10^{-09}	[−3.45, −2.25]
CI (POST–PRE) [%]	48	+13.94	13.82	+1.01	8.62×10^{-09}	3.53×10^{-09}	[+9.92, +17.95]

Table 6.1: Paired comparison between pre- and post-resistance phases for ΔD_{mean}, D_{min}, and CI. 95% CI_{mean} denotes the 95% confidence interval for the mean difference.

The introduction of inspiratory resistance produced clear and consistent modifications in venous dynamics. Across all paired acquisitions, the IVC collapsibility increased significantly ($p < 10^{-8}$), while both ΔD_{mean} and D_{min} decreased markedly (average decreases of approximately -2.16 mm and -2.85 mm, respectively). All three parameters exhibited large effect sizes ($|d_z| > 1$), confirming that the differences were not only statistically significant but also physiologically relevant.

The combination of increased collapsibility and reduced diameter indicates that inspiratory resistance enhances negative intrathoracic pressure, promoting venous return and amplifying IVC deformation during inspiration. This is consistent with the physiological response typically observed during a clinical sniff manoeuvre, but achieved here under controlled, continuous, and repeatable experimental conditions.

6.3.3 Within-posture analysis

To assess whether the effect of inspiratory resistance was posture-dependent, one-sample tests were performed separately for the NORMAL and PLR conditions. The analysis evaluated whether ΔD_{mean} differed significantly from zero within each posture. Descriptive statistics and significance levels are reported in Table 6.2.

Posture	n	**Mean [mm]**	**SD [mm]**	**Median [mm]**	**IQR [mm]**	d_z	p **(t / W)**
NORMAL	26	−2.16	1.45	−2.06	1.97	−2.10	3.1×10^{-11} / 8.3×10^{-06}
PLR	22	−1.30	1.60	−1.18	1.75	−0.81	6.0×10^{-04} / 9.8×10^{-04}

Table 6.2: One-sample tests of ΔD_{mean} within each posture. Negative values indicate a reduction in IVC mean diameter after the introduction of inspiratory resistance.

In both postures, ΔD_{mean} was significantly negative ($p < 0.01$), confirming that inspiratory resistance consistently reduced IVC diameter. However, the effect was stronger in the NORMAL posture ($d_z = -2.10$) compared with PLR ($d_z = -0.81$), suggesting that the increased preload in the PLR position partially mitigates the collapse induced by inspiratory load, stabilizing the venous segment.

6.3.4 Postural comparison

To isolate the contribution of posture to venous behaviour, paired comparisons were performed between NORMAL and PLR conditions within the same subjects, maintaining identical inspiratory resistance. The results are summarized in Table 6.3.

Variable	n_{pairs}	**Mean (NORMAL)**	**Mean (PLR)**	**Mean Diff**	SD_{diff}	d_z	p **(t / W)**
ΔD_{mean} [mm]	7	−2.98	−1.74	−1.24	0.82	−1.52	6.93×10^{-03} / 1.56×10^{-02}
$D_{\text{min,post}}$ [mm]	7	9.97	14.03	−4.06	2.98	−1.36	1.13×10^{-02} / 3.13×10^{-02}
CI_{mean} [%]	7	29.24	20.39	+8.85	9.23	+0.96	4.43×10^{-02} / 4.69×10^{-02}
CI_{post} [%]	7	40.62	26.25	+14.37	12.12	+1.19	2.01×10^{-02} / 3.13×10^{-02}

Table 6.3: Paired comparison between NORMAL and PLR postures for ΔD_{mean}, $D_{\text{min,post}}$, CI_{mean}, and CI_{post}. Differences are expressed as mean(NORMAL) − mean(PLR).

The comparison revealed statistically significant postural effects for all parameters ($p < 0.05$). In the PLR condition, both ΔD_{mean} and $D_{\text{min,post}}$ were higher and the collapsibility indices were lower. This indicates that the increased venous return associated with PLR reduces the deformation of the IVC during inspiration. Conversely, in the supine NORMAL posture, the IVC exhibited greater collapsibility and a larger reduction in diameter, consistent with lower preload and higher vessel compliance.

Overall, these results demonstrate that the proposed experimental protocol successfully induces reproducible variations in IVC diameter and collapsibility through controlled inspiratory resistance. The magnitude and direction of these effects are strongly modulated by posture: the elevation of the preload in the PLR stabilizes the IVC and attenuates respiratory fluctuations, while the supine condition amplifies them. This interaction between respiratory load and posture confirms the physiological consistency of the observed response and supports the robustness of the measurement approach.

Chapter 7

Conclusion

This study investigated the mechanical behaviour of the Inferior Vena Cava (IVC) under controlled inspiratory conditions by combining ultrasound imaging with spirometric measurements. The primary aim was to evaluate whether a standardized respiratory load could induce consistent and reproducible variations in IVC diameter, enhancing the reliability of ultrasonographic assessment compared to non-standardized breathing maneuvers.

A custom experimental setup was developed, including a 3D-printed mechanical airflow resistance designed to create a controlled inspiratory load. It also integrated a spirometer equipped with differential pressure sensors connected to a DAQ system. This setup enabled precise control of respiratory flow while ensuring synchronization with real-time ultrasound recordings acquired through the Telemed MicrUs EXT-1H system and the VIPER software.

A dedicated MATLAB pipeline was developed for data segmentation, synchronization, and quantitative analysis of IVC diameter signals. For each trial, the inspiratory phase was divided into two segments—before and after the introduction of resistance—enabling direct evaluation of the venous response to the imposed mechanical load. Quantitative parameters, including the mean and minimum diameters, diameter variation, and Caval Index (CI), were calculated to assess vessel compliance and collapsibility.

The results demonstrated a consistent reduction in IVC diameter following the application of inspiratory resistance across all subjects, with an average decrease of approximately 1 and 5 mm. This effect reflects the increase in intrathoracic pressure that opposes venous return during resisted inspiration. Moreover, the Caval Index values were systematically higher in the supine position (around 30–60%) compared to the passive leg raising (PLR) position (10–45%). These findings confirm that the PLR maneuver increases venous return and stabilizes the vessel by reducing its collapsibility. Statistical analyses confirmed these trends, revealing marked intra-subject consistency and a clear modulation of IVC dynamics by both respiratory load and posture.

Overall, the study demonstrated that controlled inspiratory resistance provides a reproducible method to elicit physiologically relevant IVC responses, offering an experimental framework for more standardized hemodynamic assessment. The combination of ultrasound imaging with synchronized spirometry proved successful in measuring venous diameter variations and could represent a valuable approach for future clinical and research applications focused on non-invasive evaluation of central venous pressure and fluid responsiveness.

7.1 Future developments

Future studies could focus on comparing the final protocol with the sniff test in clinical settings. They could also focus on expanding the subject sample and testing different resistance levels to characterize the dose-response relationship between inspiratory load and IVC behaviour. Further developments could include the integration of pressure transducers to directly measure mouth pressure or the implementation of real-time feedback algorithms to improve respiratory control. Extending the analysis to pathological populations, such as patients with heart failure or altered volume status, would validate the clinical applicability of this protocol.

Future studies could investigate different airflow targets to identify a respiratory pattern that is even more general and physiologically representative than the approach adopted in the present work. Refining the target flow could improve both the repeatability of the maneuver and its adaptability for subjects with varying respiratory abilities.

The integration of a Lower Body Negative Pressure (LBNP) system could represent an innovative extension of this work. LBNP devices enable precise simulation of central hypovolemia by progressively reducing venous return from the lower body. Combining LBNP with the current ultrasound and spirometric setup could allow a more comprehensive assessment of the hemodynamic response of the IVC under different preload conditions. This approach could help quantify the sensitivity of IVC-based indices to changes in central blood volume, contributing to the development of non-invasive indicators for monitoring fluid status and cardiovascular health.

Appendix A

Minimum Diameter and CI Graphs

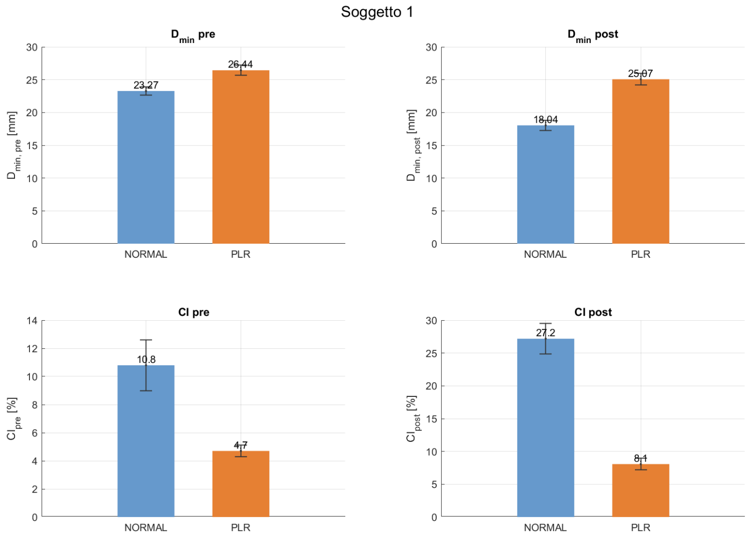

Figure A.1: Bar plot of minimum diameter and inspiration-only CI for pre and post-resistance, for subject 1

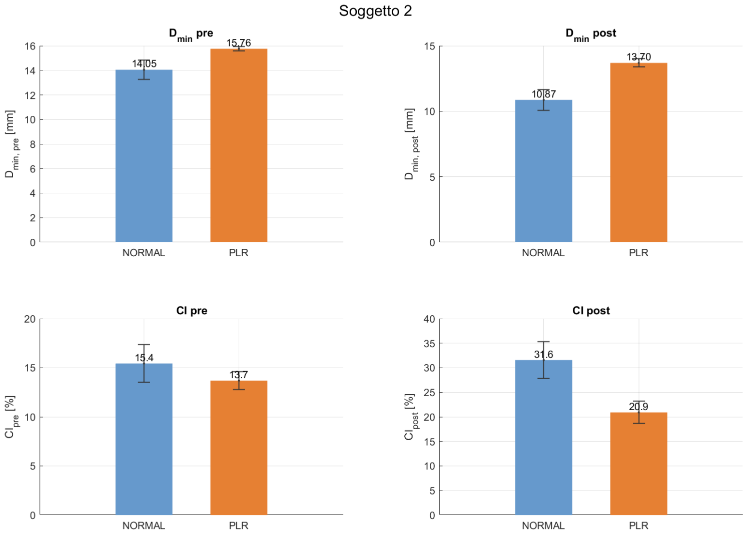

Figure A.2: Bar plot of minimum diameter and inspiration-only CI for pre and post-resistance, for subject 2

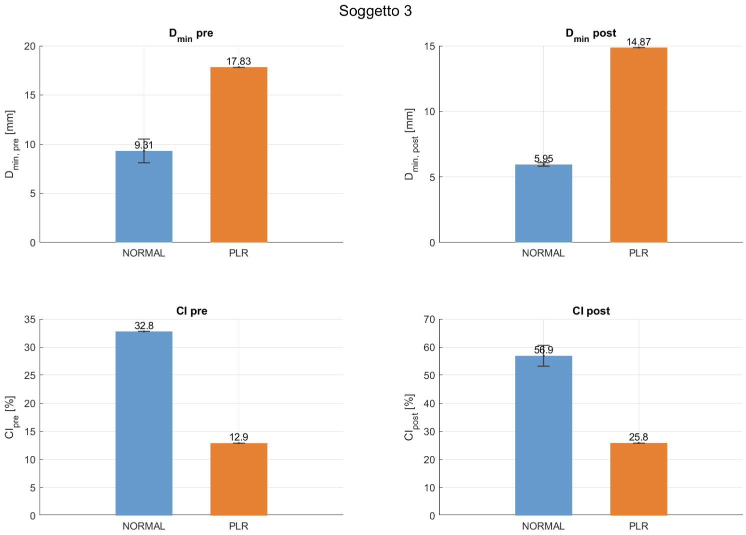

Figure A.3: Bar plot of minimum diameter and inspiration-only CI for pre and post-resistance, for subject 3

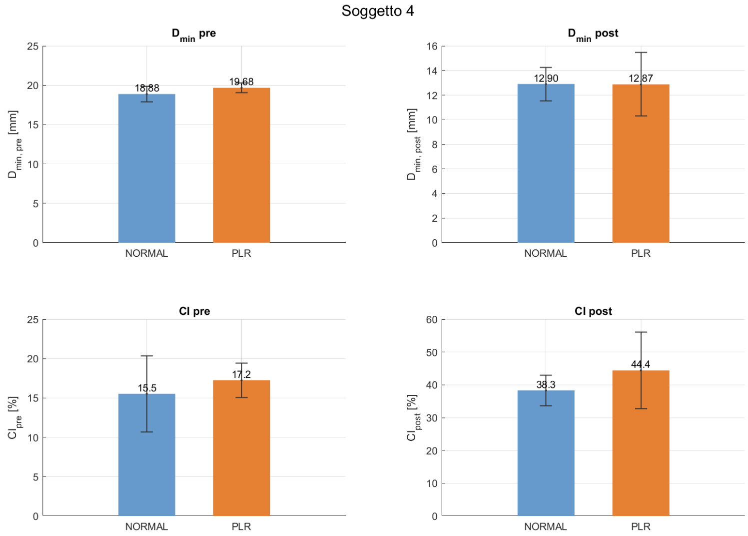

Figure A.4: Bar plot of minimum diameter and inspiration-only CI for pre and post-resistance, for subject 4

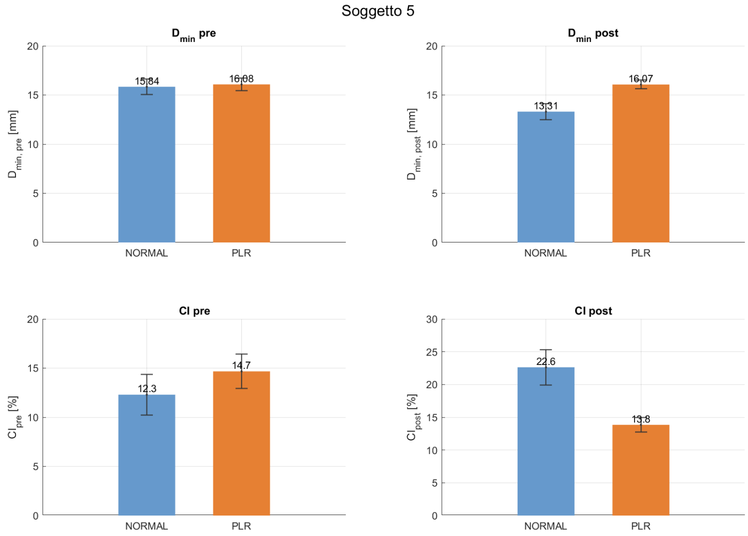

Figure A.5: Bar plot of minimum diameter and inspiration-only CI for pre and post-resistance, for subject 5

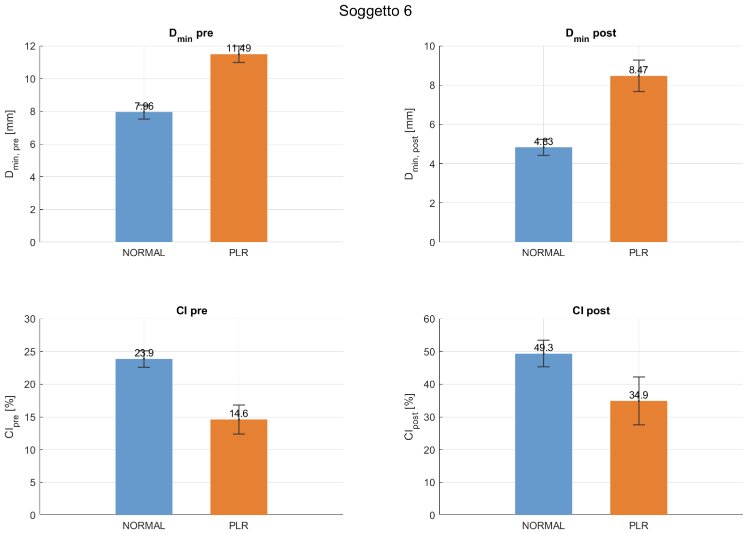

Figure A.6: Bar plot of minimum diameter and inspiration-only CI for pre and post-resistance, for subject 6

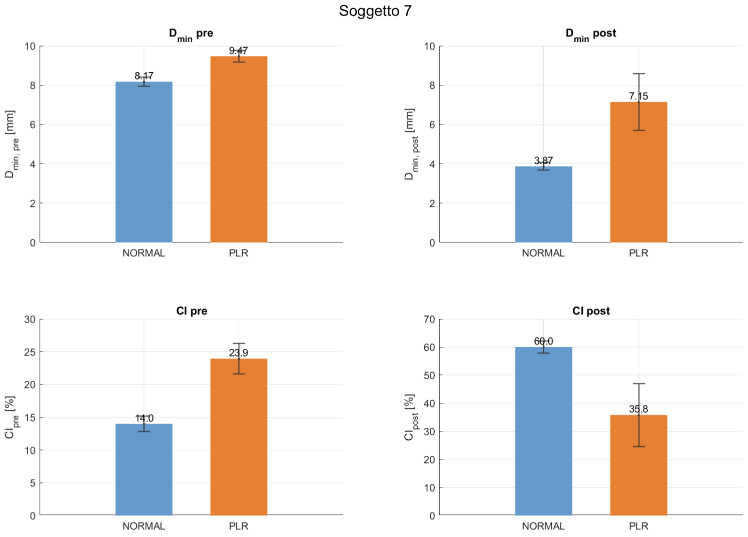

Figure A.7: Bar plot of minimum diameter and inspiration-only CI for pre and post-resistance, for subject 7

Appendix B

Global CI Graphs

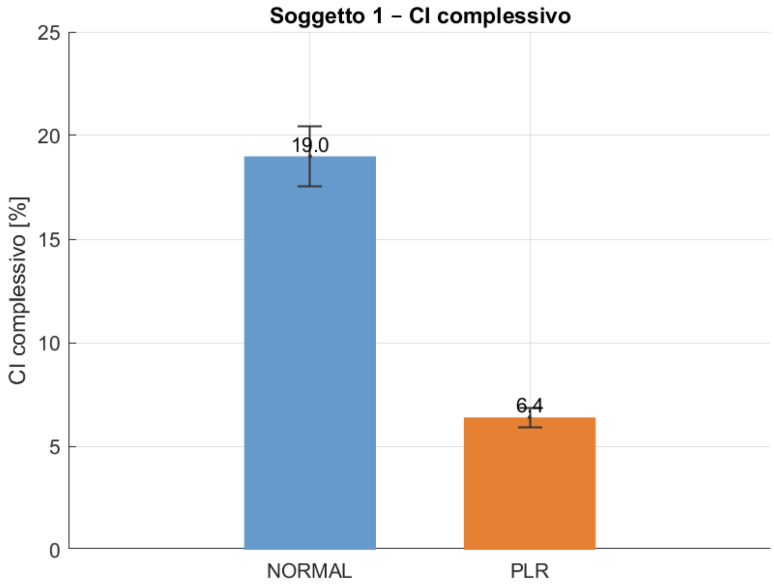

Figure B.1: Bar plot of global CI for subject 1

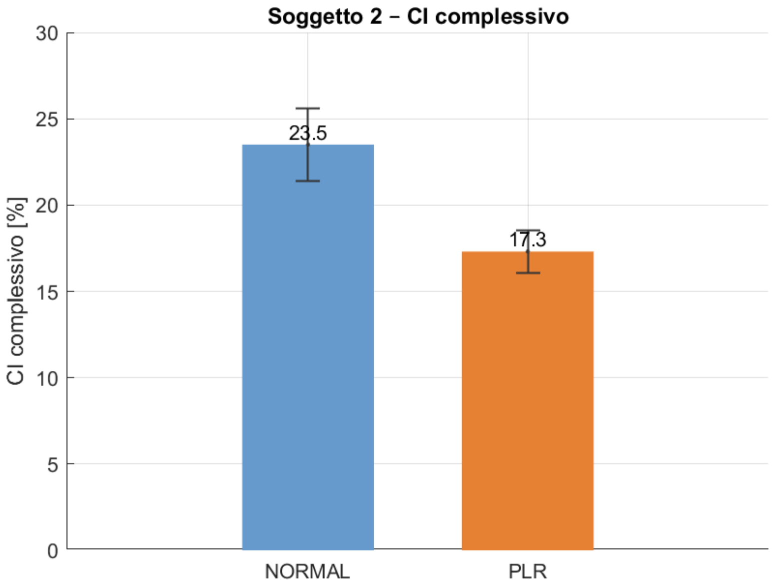

Figure B.2: Bar plot of global CI for subject 2

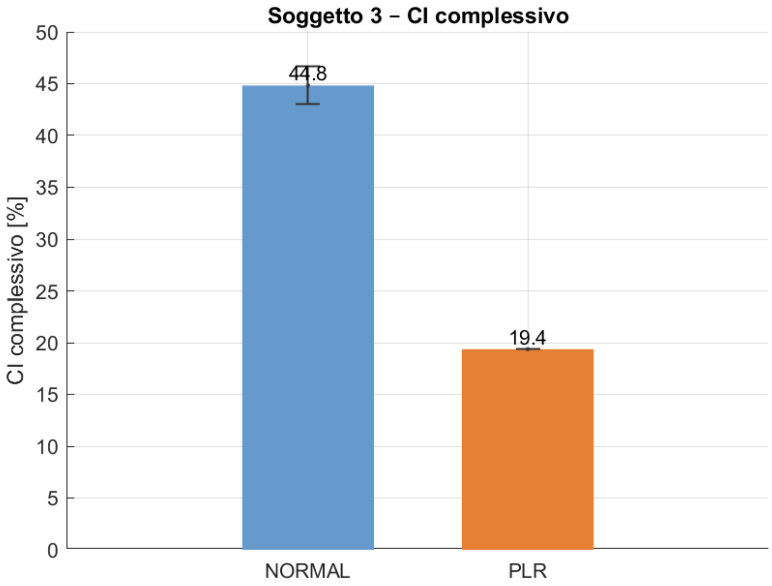

Figure B.3: Bar plot of global CI for subject 3

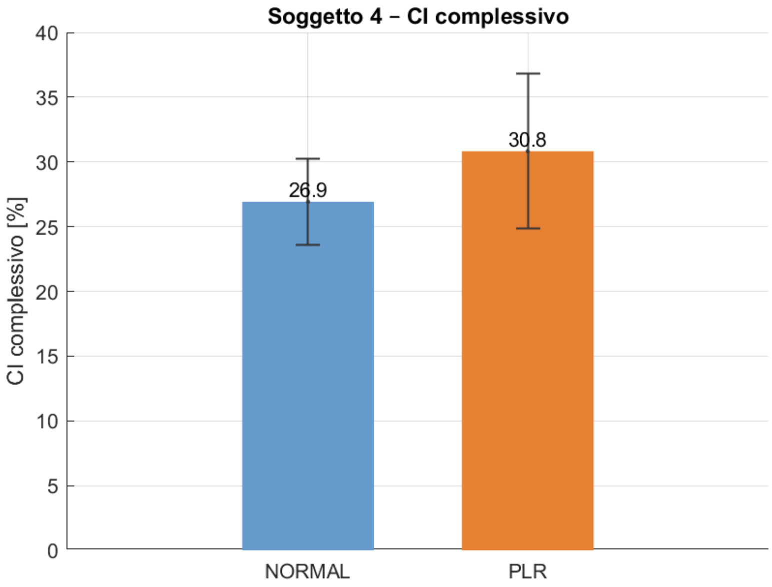

Figure B.4: Bar plot of global CI for subject 4

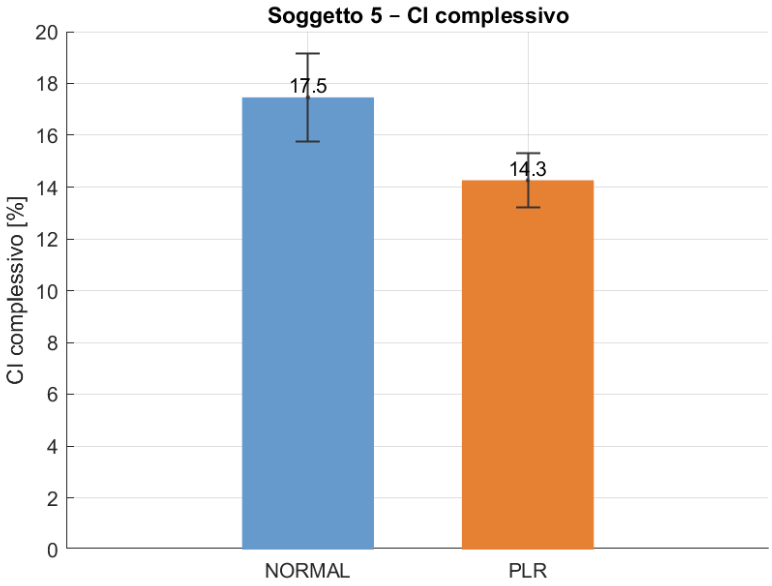

Figure B.5: Bar plot of global CI for subject 5

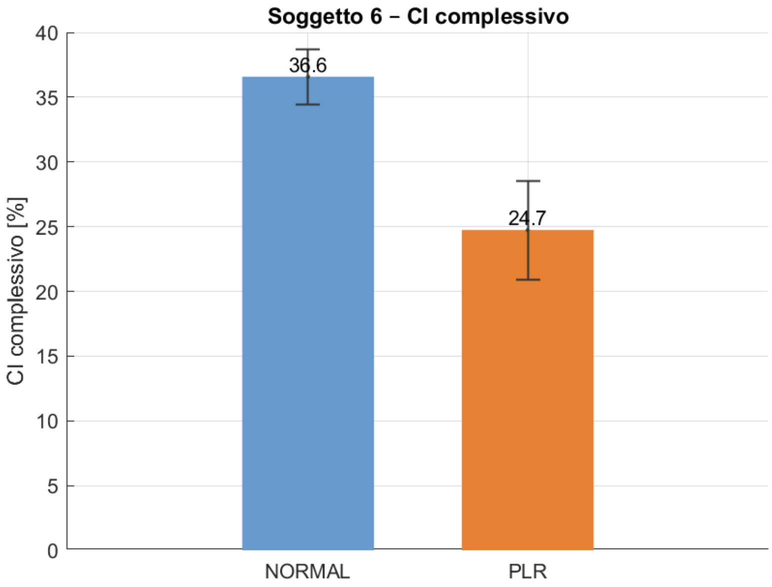

Figure B.6: Bar plot of global CI for subject 6

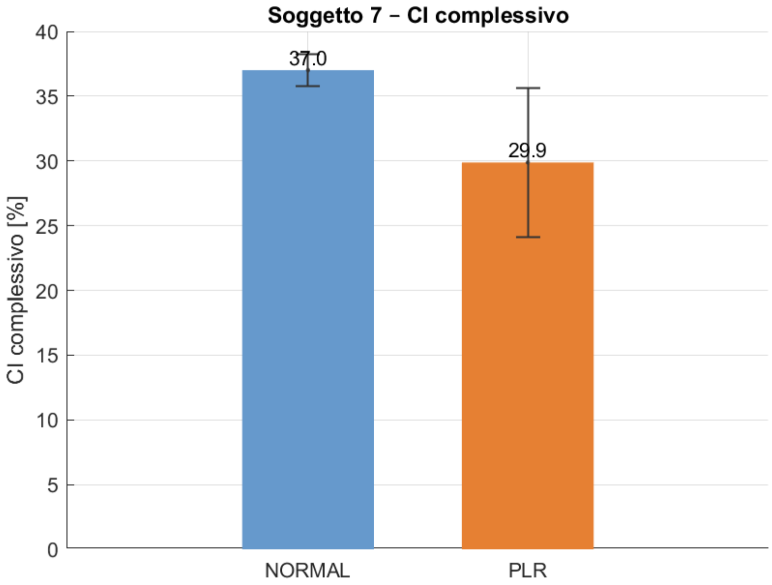

Figure B.7: Bar plot of global CI for subject 7

Appendix C

Variation of Diameter between Postures

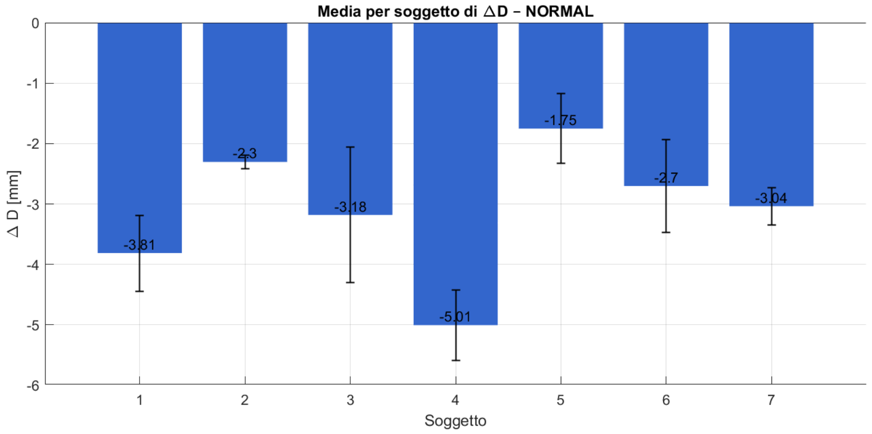

Figure C.1: Bar plot of variation of diameter in supine position, for all subjects

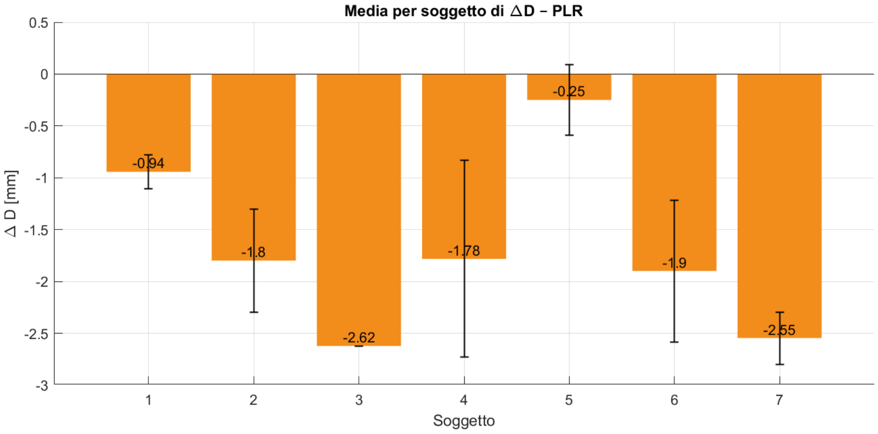

Figure C.2: Bar plot of variation of diameter in PLR position, for all subjects

Bibliography

[1] P. D. Nicolò, G. Tavazzi, L. Nannoni, and F. Corradi, “Inferior vena cava ultrasonography for volume status evaluation: an intriguing promise never fulfilled,” *Journal of Clinical Medicine*, vol. 12, no. 6, p. 2217, 2023.

[2] P. Policastro, G. Chiarion, F. Ponzio, L. Ermini, S. Civera, S. Albani, G. Musumeci, S. Roatta, and L. Mesin, “Detection of inferior vena cava in ultrasound scans through a deep learning model,” *Electronics*, vol. 12, no. 7, p. 1725, 2023.

[3] C. L. Stanfield, *Principles of Human Physiology*. Benjamin-Cummings Pub Co, 2017.

[4] C. S. Borowy and T. Mukhdomi, “Sonography physical principles and instrumentation,” Mar. 2023. StatPearls Publishing. `https://www.ncbi.nlm.nih.gov/books/NBK567710/`.

[5] W. D. Tucker, R. Shrestha, and B. Burns, “Anatomy, abdomen and pelvis: Inferior vena cava,” *StatPearls [Internet]*, 2023. Last update: July 24, 2023. Available from: `https://www.ncbi.nlm.nih.gov/books/NBK537201/`.

[6] S. Albani, L. Mesin, S. Roatta, A. De Luca, A. Giannoni, D. Stolfo, L. Biava, C. Bonino, L. Contu, E. Pelloni, E. Attena, V. Russo, F. Antonini-Canterin, N. R. Pugliese, G. Gallone, G. M. De Ferrari, G. Sinagra, and P. Scacciatella, “Inferior vena cava edge tracking echocardiography: A promising tool with applications in multiple clinical settings,” *Diagnostics*, vol. 12, no. 2, p. 427, 2022.

[7] M. F. Lutfi, “The physiological basis and clinical significance of lung volume measurements,” *Multidisciplinary Respiratory Medicine*, vol. 12, no. 3, pp. 1–6, 2017.

[8] A. C. Egbe, H. M. Connolly, P. A. Pellikka, J. H. Anderson, and W. R. Miranda, “Role of inferior vena cava dynamics for estimating right atrial pressure in congenital heart disease,” *Circulation: Cardiovascular Imaging*, vol. 15, no. 9, p. e014308, 2022.

[9] T. L. Szabo, *Diagnostic Ultrasound Imaging: Inside Out*. Academic Press, 2nd ed., 2014.

[10] J. A. Jensen, “Field ii (version 3) a program for simulating ultrasound systems,” *Medical and Biological Engineering and Computing*, vol. 34, no. 1, pp. 351–353, 1996.

[11] Z. Hindi and Y. Fares, “Common artifacts in ultrasonography: A pictorial review,” *Ultrasound*, vol. 20, no. 1, pp. 25–38, 2012.

[12] R. P. Smillie, M. Shetty, N. Boycott, and S. Ghai, “Understanding and recognizing ultrasound artifacts,” *RadioGraphics*, vol. 35, no. 7, pp. 2009–2024, 2015.

[13] L. Mesin, Y. Long, A. Scano, A. Barone, M. Righi, M. Prato, A. Porta, P. Cavallari, and F. Toso, “Automatic measurement of the inferior vena cava diameter in

ultrasound imaging by means of an active contour model," *Computerized Medical Imaging and Graphics*, vol. 46, pp. 36–47, 2015.

[14] P. Di Nicolò, G. Ghigliotti, R. Urso, *et al.*, "Inferior vena cava ultrasonography for volume status assessment in the critically ill," *Critical Care*, vol. 27, no. 1, p. 100, 2023.

[15] W. Ciozda, I. Kedan, D. W. Kehl, R. Zimmer, R. Khandwalla, and A. Kimchi, "The efficacy of sonographic measurement of inferior vena cava diameter as an estimate of central venous pressure," *Journal of Intensive Care Medicine*, vol. 31, no. 6, pp. 333–343, 2016.

[16] S. Mittal and A. Kumar, "Inferior vena cava ultrasound for volume status evaluation: A conundrum," *Journal of Current Cardiology*, vol. 3, pp. 12–17, January–April 2025.

[17] M. Kaptein, I. van der Horst, P. van den Berg, and et al., "Clinical use of inferior vena cava ultrasound: Review and critical appraisal of current evidence," *Ultrasound Journal*, vol. 15, no. 1, p. 10, 2023.

[18] P. Policastro, L. Ermini, S. Civera, S. Albani, G. Musumeci, S. Roatta, and L. Mesin, "Effect of respirophasic displacement of the inferior vena cava on size measurement in 2-d ultrasound imaging," *Ultrasound in Medicine & Biology*, vol. 56, pp. 1–10, 2024.

[19] Y. Chikata, M. Izawa, A. Takeda, N. Okuda, and H. Imanaka, "Evaluation of a newly developed flow-transducing spirometer with a venturi-type flow sensor," *BioMedical Engineering OnLine*, vol. 13, no. 1, p. 84, 2014.

[20] Sensirion AG, "Sdp800 series – differential pressure sensors." `https://sensirion.com/products/catalog/SDP800-125Pa`.

[21] National Instruments, "Usb-6001 specifications." `https://www.ni.com/it-it/shop/model/usb-6001.html`.

[22] Telemed Ultrasound, "Micrus ext-1h: Portable usb ultrasound system." `https://www.telemedultrasound.com/products/micrus-scanner/`.

[23] Telemed Medical Imaging Solutions, *Telemed Ultrasound Systems Product Brochure*, 2023.

[24] I. Ciesielski, M. Corbally, C. Liew, J. Kehoe, C. Dinsmore, and R. Dinsmore, "Advanced point-of-care ultrasound from the trauma bay to the ward: Expanding applications and best practice," *Diagnostics*, vol. 15, no. 2, p. 520, 2025.

[25] D. C. Montgomery and G. C. Runger, *Applied Statistics and Probability for Engineers*. Wiley, 7th ed., 2018.